

(Abstract:

words)

Graphical Abstract

Prestimulus neural population dynamics predict RT but not choice during perceptual decisions - further generalizing the initial condition hypothesis

Pierre Boucher, Tian Wang, Laura Carceroni, Gary Kane, Krishna V Shenoy, Chandramouli Chandrasekaran



Highlights

Prestimulus neural population dynamics predict RT but not choice during perceptual decisions - further generalizing the initial condition hypothesis

Pierre Boucher, Tian Wang, Laura Carceroni, Gary Kane, Krishna V Shenoy, Chandramouli Chandrasekaran

- Prestimulus spiking activity is predictive of RT but not choice
- Prestimulus dynamics covary with the outcome of previous trials
- Initial condition hypothesis is a useful framework through which to understand decision-making population dynamics

Prestimulus neural population dynamics predict RT but not choice during perceptual decisions - further generalizing the initial condition hypothesis

Pierre Boucher^a, Tian Wang^a, Laura Carceroni^c, Gary Kane^c, Krishna V Shenoy^{e,f,g,h,i,j}, Chandramouli Chandrasekaran^{a,b,c,d}

^a*Department of Biomedical Engineering, Boston University, Boston, 02115, MA, USA*

^b*Department of Anatomy & Neurobiology, Boston University, Boston, 02118, MA, USA*

^c*Department of Psychological and Brain Sciences, Boston University, Boston, 02115, MA, USA*

^d*Center for Systems Neuroscience, Boston University, Boston, 02115, MA, USA*

^e*Department of Electrical Engineering, Stanford University, Stanford, 94305, CA, USA*

^f*Department of Neurobiology, Stanford University, Stanford, 94305, CA, USA*

^g*Howard Hughes Medical Institute, HHMI, Chevy Chase, 20815-6789, MD, USA*

^h*Department of Bioengineering, Stanford University, Stanford, 94305, CA, USA*

ⁱ*Stanford Neurosciences Institute, Stanford University, Stanford, 94305, CA, USA*

^j*Bio-X Program, Stanford University, Stanford, 94305, CA, USA*

Abstract

The link between neural population dynamics in decision-related brain regions and decision-making behavior is a fundamentally unresolved problem. Here, we investigated if the “initial condition hypothesis”, originally conceived in studies of motor planning and refined in timing studies, could bridge the gap between decision-related dynamics and behavior. The initial condition hypothesis posits that the speed and location of post-stimulus neural population dynamics and behavior is substantially determined by the prestimulus state (i.e., the initial condition). We tested this hypothesis by investigating neural population dynamics of neurons recorded from the dorsal premotor cortex, a key decision-related brain region, of monkeys performing a red-green reaction time (RT) checkerboard discrimination task. Dimensionality reduction, trajectory analysis, and decoding revealed that prestimulus neural state indeed predicted the evolution of post-stimulus neural trajectories (speed and location) and behavior, specifically but not eventual choice. Furthermore, faster RTs were associated with faster pre- and post-stimulus dynamics as compared to slower RTs, **with these effects observed within a stimulus difficulty**. Such alterations in prestimulus population state and dynamics were at least in part explained by the outcome of the previous trial, with generally slower pre- and post-stimulus population dynamics and RTs on trials following an error as compared to trials following a correct response. Finally, cognitive process modeling suggested decision-related dynamics and behavior is most consistent with a gain signal that varied on a trial-by-trial basis. Together these results suggest that the initial condition hypothesis is a powerful perspective to understanding the neural population dynamics underlying decision-making. Together these results suggest similar mechanisms from motor planning and timing may form the basis for decision-making, further generalizing the initial condition hypothesis.

Keywords: Population Dynamics, Decision-making, Dorsal Premotor Cortex, Urgency, Modeling, Initial Condition Hypothesis

1. Introduction

There are 10 minutes to make it to the airport but the GPS says you're still 12 minutes away. Seeing a yellow light in the distance you quickly floor it. You get to the intersection only to realize you have run a red light. The sight of the lights result in patterns of neural activity that respectively lead you to respond quickly to your environment (i.e., speed up when you see the yellow) and process feedback (i.e., slow down after running the red). This process of choosing, performing, and altering actions in response to sensory cues and context is termed perceptual decision-making (Cisek, 2012; Kiani et al., 2013; Brody and Hanks, 2016; Gold and Shadlen, 2007; Brunton et al., 2013).

Research in invertebrates (Briggman et al., 2005; Kato et al., 2015), rodents (Hanks et al., 2015; Guo et al., 2014), monkeys (Roitman and Shadlen, 2002; Churchland et al., 2008), and humans (Pereira et al., 2021; Kelly and O'Connell, 2013) has attempted to understand the neural basis for decision-making. Barring few exceptions (Okazawa et al., 2021; Mante et al., 2013; Thura et al., 2020), emphasis has been placed on understanding how processes such as evidence accumulation and 'urgency' are represented in single neuron responses in decision-related brain regions (Roitman and Shadlen, 2002; Churchland et al., 2008; Thura and Cisek, 2014). However, how these processes manifest in neural population dynamics to mediate decision-making behavior, especially in reaction time (RT) tasks, is largely unclear. We address this gap by investigating if the "initial condition" hypothesis, originally posited in motor planning studies, subsumes decision-related dynamics and behavior (Churchland et al., 2006b; Afshar et al., 2011).

Studies of motor planning, timing, speed-accuracy tradeoff (SAT) and post-error adjustment all suggest that the neural population state before a cue, that is the *initial condition*, largely predicts the speed of subsequent neural dynamics and behavioral response. For example, the state and speed of the neural population dynamics (i.e., initial condition) at the time of the 'go' cue explained considerable variability in RTs (Afshar et al. 2011, see Fig 1A). Similarly, in studies of timing, the initial condition encoded the perceived time interval and predicted the speed of subsequent neural dynamics and the reproduced time interval (Remington et al. 2018, see Fig 1B). Finally, in SAT and post-error adjustment experiments, prestimulus neural activity, a proxy for the initial condition, is different for fast vs. slow blocks and depends on the outcome of the previous trial respectively (Murphy et al. 2016; Bogacz et al. 2010; Purcell and Kiani 2016; Thura et al. 2017, see Fig 1C). Together this evidence suggests that for decision-making, the initial condition, that is the prestimulus neural population state, will predict post-stimulus decision-related neural dynamics and behavior. Pre-stimulus state will either predict both RT and choice (Fig 1D) or RT only (Fig 1E). In both cases, the prestimulus neural population state is dependent upon previous trial outcomes.

We tested this initial condition hypothesis (Afshar et al., 2011; Churchland et al., 2010, 2006b) by examining firing rates of neurons recorded in dorsal premotor cortex (PMd) of monkeys performing a red-green RT perceptual decision-making task (Chandrasekaran et al., 2017). We found that decision-related dynamics in PMd were indeed consistent with the initial condition hypothesis. First, analysis of the "representational" geometry using state space trajectories organized by RT suggested that neural population dynamics were spatially separated pre- and post-stimulus as a function of RT. Subsequent analysis of the dynamics of these trajectories suggested that faster RTs were associated with faster pre- and post-stimulus dynamics as compared to slower RTs. We also found that the excursion from the pre-stimulus state to the movement initiation state depended on RT. Both effects were observed within

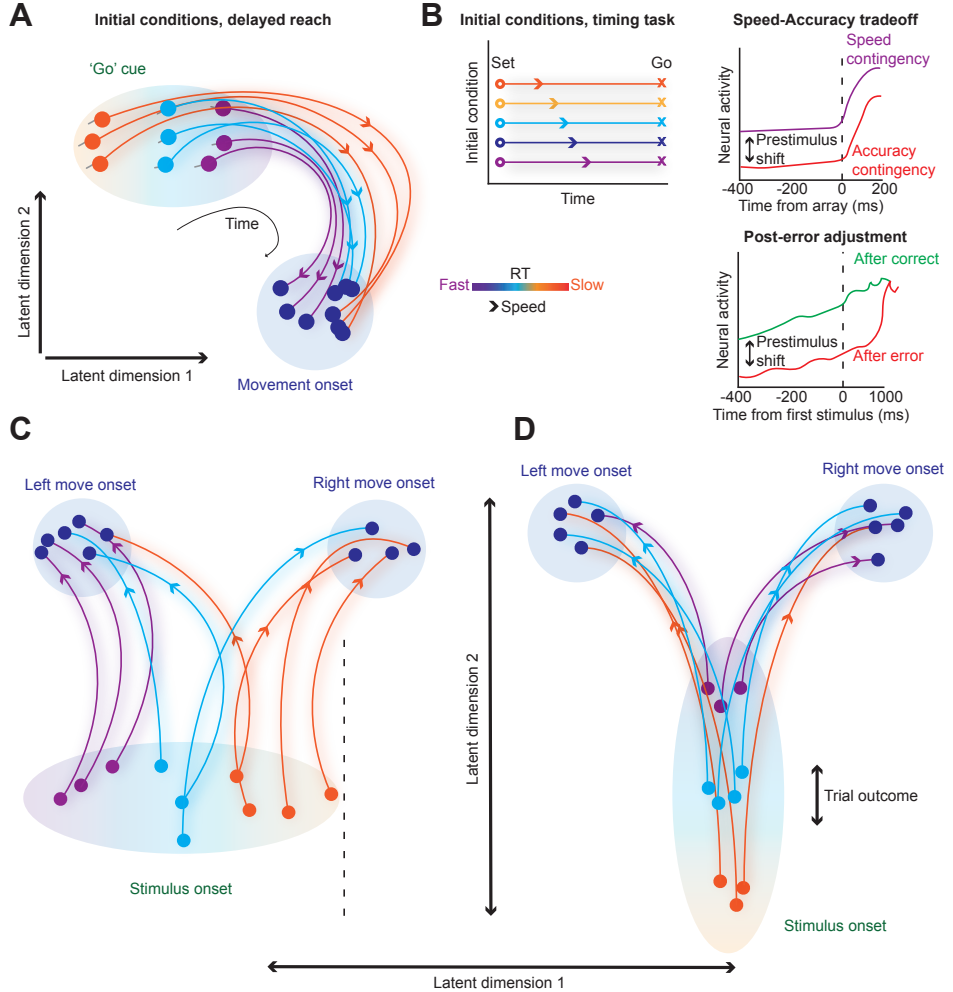


Figure 1: Initial conditions predict subsequent neural dynamics and behavior **(A)** Initial condition hypothesis from delayed reach experiments (Afshar et al., 2011) posits that the neural state immediately preceding a 'go' cue predict the location and speed of a state space trajectory, leading to faster RTs if the initial conditions are closer to a movement onset state. Dots within the ellipses denote population states, and the lines hypothetical trajectories through state space. **(B)** The neural population state at the end of a perceived time interval is organized by the perceived time interval, and is related to the speed of subsequent dynamics and behavior. (the reproduced time intervals Remington et al., 2018). **(C)** Pre-stimulus neural activity differs for speed and accuracy contingencies for speed-accuracy tradeoff tasks. (top Heitz and Schall, 2012) or after correct and error trials (bottom Thura et al., 2017). **(D)** Hypothesis 1: Biased initial conditions predict both RT and choice. Initial state varies trial-to-trial, and is biased towards one choice, here left. Trials closer to the left choice will have faster RTs and RTs will be slower for right choices. In this model, pre-stimulus state would predict *both* RT and choice, and minimal effects of trial outcome. **(E)** Hypothesis 2: Initial conditions predict RT only. Pre-stimulus dynamics are faster and closer to the movement initiation state for faster (purple) compared to slower RTs (orange). Prestimulus state is outcome dependent in that correct or error trials shift initial conditions to either eventual faster or slower RT states. In **A**, **C**, & **D** Ellipses indicate the variability of state space for stimulus/go and movement onset respectively. Purple to orange gradients represent RT variability from fast to slow.

a stimulus difficulty. Bolstering these PCA observations, decoding and regression analyses revealed that prestimulus neural state only predicted RT but not the eventual choice (Fig 1E). Finally, we found that prestimulus population dynamics and RTs depended on the outcome of the previous trial: Pre- and post-stimulus dynamics were slower on trials following an error as compared to trials following a correct response. We built cognitive process models based on these neural results and examined if inclusion of a variable gain signal better described decision-making behavior. We found that models armed with a linear or nonlinear multiplicative gain signal with an intercept and a slope that varied on a trial-by-trial basis provided a powerful description of the data and was better than models without a variable gain signal. All gain signal models were better than models without gain signals.

Together these results strongly support a dynamical view of decision-making where the initial condition contributes at least in part to subsequent dynamics and behavior. This initial condition and subsequent dynamics are likely controlled by a gain signal that varies on a trial-by-trial basis. More broadly, these results suggest a unified dynamical mechanism may underlie motor planning, decision-making and timing.

(Introduction: 693 words)

2. Results

2.1. Reaction times are variable during decision-making even for easy decisions

We trained two macaque monkeys (O. and T.) to discriminate the dominant color of a central, static checkerboard composed of red and green squares and to report their decisions with arm movements (Fig 2A). Fig. 2B depicts the trial timeline. The trial began when the monkey held the center target and fixated on the fixation cross. After a short randomized holding time (300-485 ms), a red and a green target appeared on either side of the central hold (target configurations were randomized). After an additional randomized target viewing time drawn from a censored exponential distribution (400-1000 ms), the checkerboard appeared. The monkey's task was to discriminate the dominant color in the checkerboard and reach to and touch the target matching the dominant color of the checkerboard.

There were seven levels of stimulus difficulty parametrized by unsigned coherence (' C ', Fig 2C). ' C ' is independent of the actual dominant color and is the absolute difference in the number of red (R) and green (G) squares normalized by the total number of squares in the checkerboard ($C = 100 \times \frac{|R-G|}{(R+G)}$). Signed color coherence (SC), dependent on the actual dominant color of the checkerboard, is defined as $SC = 100 \times \frac{R-G}{(R+G)}$. While animals performed the task, we measured the arm and eye movements of the monkeys. RTs were identified as the first time when hand speed exceeded 10% of maximum speed during a reach.

The behavioral performance of the monkeys depended on the difficulty of the discrimination (i.e., color coherence). In general, across all sessions, monkeys made more errors when discriminating stimuli with near equal combinations of red and green squares (Fig 2D). We fit the proportion correct as a function of unsigned coherence using a Weibull function to estimate slopes and psychometric thresholds (average R^2 ; T=0.99 (over 75 sessions); O: 0.99 (over 66 sessions); slope (β , M± SD over sessions, T: 1.30 ± 0.16 , O: 1.22 ± 0.16). Monkey T was more sensitive than monkey O in discriminating the color of the checkerboards (thresholds are computed on a per session basis and averaged over sessions at 81.6% correct, (M ± SD): T: $10.76 \pm 1.27\%$, O: $15.42 \pm 1.84\%$, Wilcoxon rank sum comparing median thresholds, $p= 2.91e-23$).

As expected, monkeys were generally slower for more ambiguous checkerboards. However, as the box plots in Fig. 2F show, a key feature of decision-making behavior is that RTs are quite variable even for the easiest coherences. A regression analysis between $\log(C)$ and RT only explained ~12.5% and ~1.5% of RT variability in monkeys T and O. These regression results suggest that there is rich variability in RTs and we investigated if the initial condition hypothesis can explain such variability.

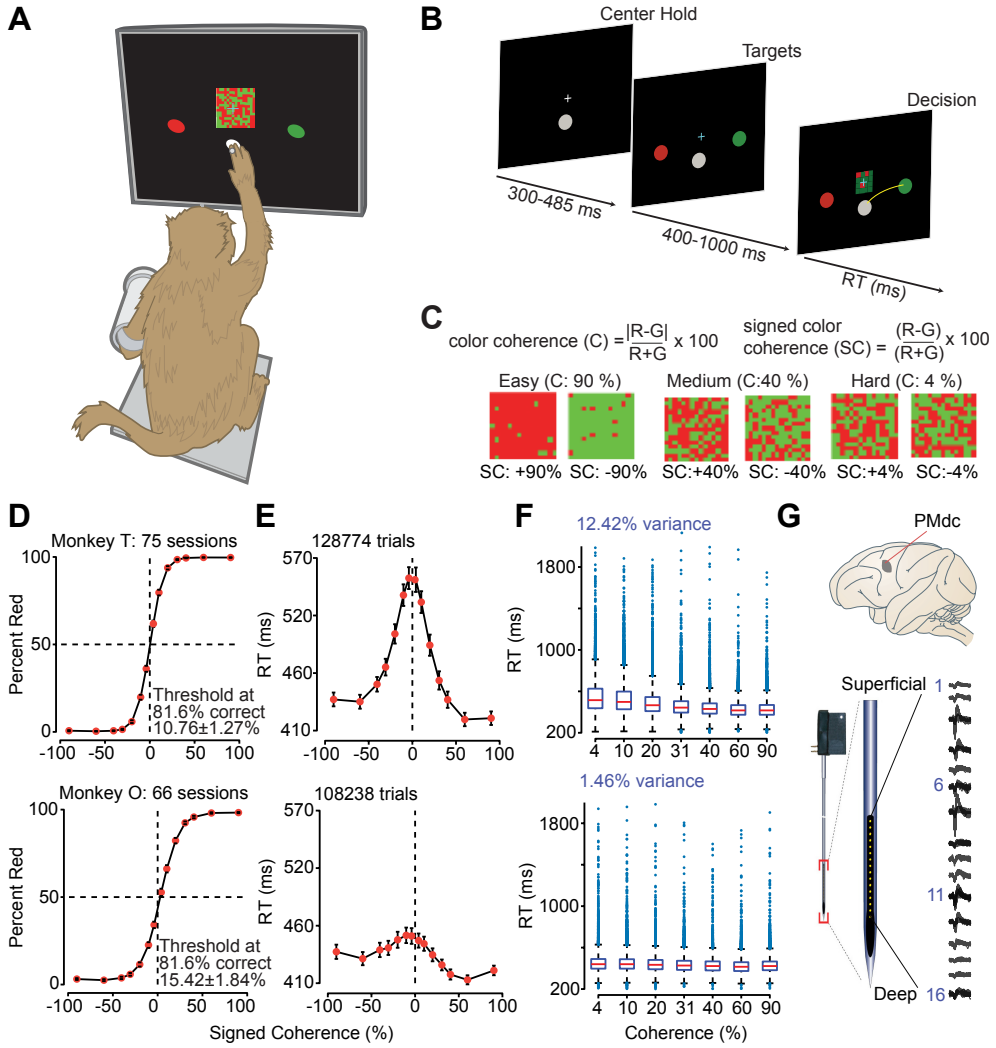


Figure 2: Monkeys can discriminate red-green checkerboards and demonstrate rich variability in RTs between and within stimulus coherences (A) An illustration of the setup for the behavioral task. We loosely restrained the arm the monkey was not using with a plastic tube and cloth sling. A reflective infrared bead was taped on the middle digit of the active hand to be tracked in 3D space. We used the measured hand position to mimic a touch screen and to provide an estimate of instantaneous arm position; eye position was tracked using an infrared reflective mirror placed in front of the monkey's nose. (B) Timeline of the discrimination task. (C) Examples of different stimuli used in the experiment parameterized by the color coherence of the checkerboard cue. Positive values of signed coherence(SC) denote more red (R) than green (G) squares and vice versa. (D) Psychometric curves, percent responded red, and (E) RTs (correct and incorrect trials) as a function of the percent SC of the checkerboard cue, over sessions of the two monkeys (T: 75 sessions; O: 66 sessions). Dark orange markers show measured data points along with $2 \times SEM$ estimated over sessions (D, error bars lie within the marker for many data points). The black line segments are drawn in between these measured data points to guide the eye. (D) Discrimination thresholds, the color coherence level at which the monkey made 81.6% correct choices, are also shown. (F) Box-and-whisker plot of RT as a function of unsigned checkerboard coherence. Outliers are plotted as blue circles. There is large variation of RTs both across and within coherences. (G) Location of caudal PMd (PMdc, location of electrode implantation) along with an example recording from a 16 electrode, 150- μm spacing U-probe (Plexon, Inc., Dallas, TX, United States). The brain in this figure is adapted from ([Ghazanfar and Santos, 2004](#)).

2.2. PMd neurons demonstrate complex time-varying patterns of firing rates

Our database for understanding the neural population dynamics underlying decision-making consisted of 996 units (546 units in T and 450 units in O, including both single neurons and multi-units, 801 single neurons) recorded from PMd of the two monkeys over 141 sessions. Chosen units were included as they were well isolated from other units/separated from noise and modulated activity in at least one task epoch. Single neurons were identified by a combination of spike sorting as well as analysis of inter-spike-intervals, with neurons having ISI distributions of $1.5\% < 1.5$ ms. ([Fig. 3](#)) shows the firing rates of six example units recorded in PMd aligned to checkerboard onset and organized by coherence and choice ([Fig 3A](#)) or organized by RT and choice ([Fig 3B](#)). For the coherence data, firing rates were plotted until the median RT, and for the RT data, firing rates were plotted until the midpoint of RT bin range.

PMd neurons demonstrated heterogeneous patterns of firing rates that covary with coherence, choice, and RT suggesting that they were likely a component of the decision formation process. Many neurons showed reassuring and classical ramp-like firing rates documented previously ([Shadlen and Newsome 1996, 2001; Roitman and Shadlen 2002; Hanks et al. 2014; Latimer et al. 2015](#), see [Fig 3](#), top 3 rows). However, many other neurons showed heterogeneous and complex patterns of activity that included both task-related increases and decreases in firing rate ([Fig 3](#), bottom 3 rows). We previously utilized a variety of single neuron metrics to systematically and exhaustively describe these different neural populations ([Chandrasekaran et al., 2017](#)).

Remarkably, despite temporal complexity and heterogeneity, almost all of these albeit selected neurons demonstrate prestimulus firing rate covariation with RT consistent with the predictions of the initial condition hypothesis. In the next two sections, we use PCA to further interrogate how RT and choice were represented in the shared activity of these neurons and if initial conditions predicted various facets of decision-making behavior.

2.3. The initial condition before stimulus onset predicts RT but not choice

Current models of decision-making emphasize that RT variability should be mostly driven by the amount of stimulus evidence. However, stimulus evidence accounts for maximally $\sim 12.5\%$ of the variance and there is considerable RT variability even within a stimulus difficulty and ([Fig 2F](#)). So, what accounts for RT variability even within a stimulus difficulty? We hypothesized that the initial conditions, or population neural dynamics just before stimulus onset, should strongly account for this variability as they should covary with RT and this effect should be observed within a stimulus difficulty.

To test this hypothesis, we performed a principal component analysis (PCA) on trial-averaged firing rate activity (smoothed with a 30 ms Gaussian) windowed about checkerboard onset, organized by RT bins, 11 levels representing a spectrum from faster to slower RTs (300-400 ms, to 600-1000 ms), and both reach directions ([Fig 4A & B](#)). We used the approach developed in Machens et al. 2010 to estimate the *signal+noise* and *noise* variances. Standard error for the *signal+noise* PCA was estimated through bootstrapping over trials (50 repeats). We then excluded dimensions where the *signal+noise* variance was significantly lower than the *noise* variance and performed further analysis on the other dimensions. This analysis yielded 6 principal components (PCs) that explained $> 90\%$ of the variance in firing rates ([Fig 4A](#)).

The first 3 PCs of population firing rate activity after stimulus onset separate as a function of choice and RT bin when plotted in state space ([Fig 4D](#)). Note, in a PCA organized by coherence and choice, activity separated faster for easier compared to harder coherences ([SFig 1B](#)). Both these results provide a population level replication of the classical studies of single neurons ([Shadlen and Newsome, 2001; Roitman and Shadlen, 2002; Ding and Gold, 2010](#)).

Besides covariation with choice and RT after stimulus onset, what is apparent is that PCs 1, 3, and 4 ([Fig 4A](#)) separate by RT even before stimulus onset. We visualized in the first, second, and fourth PCs in state space ([Fig 4B](#)). In these trajectories, the small squares denote 20 ms steps in time.

In this state space plot, both position and speed of the pre-stimulus state covaries with RT.

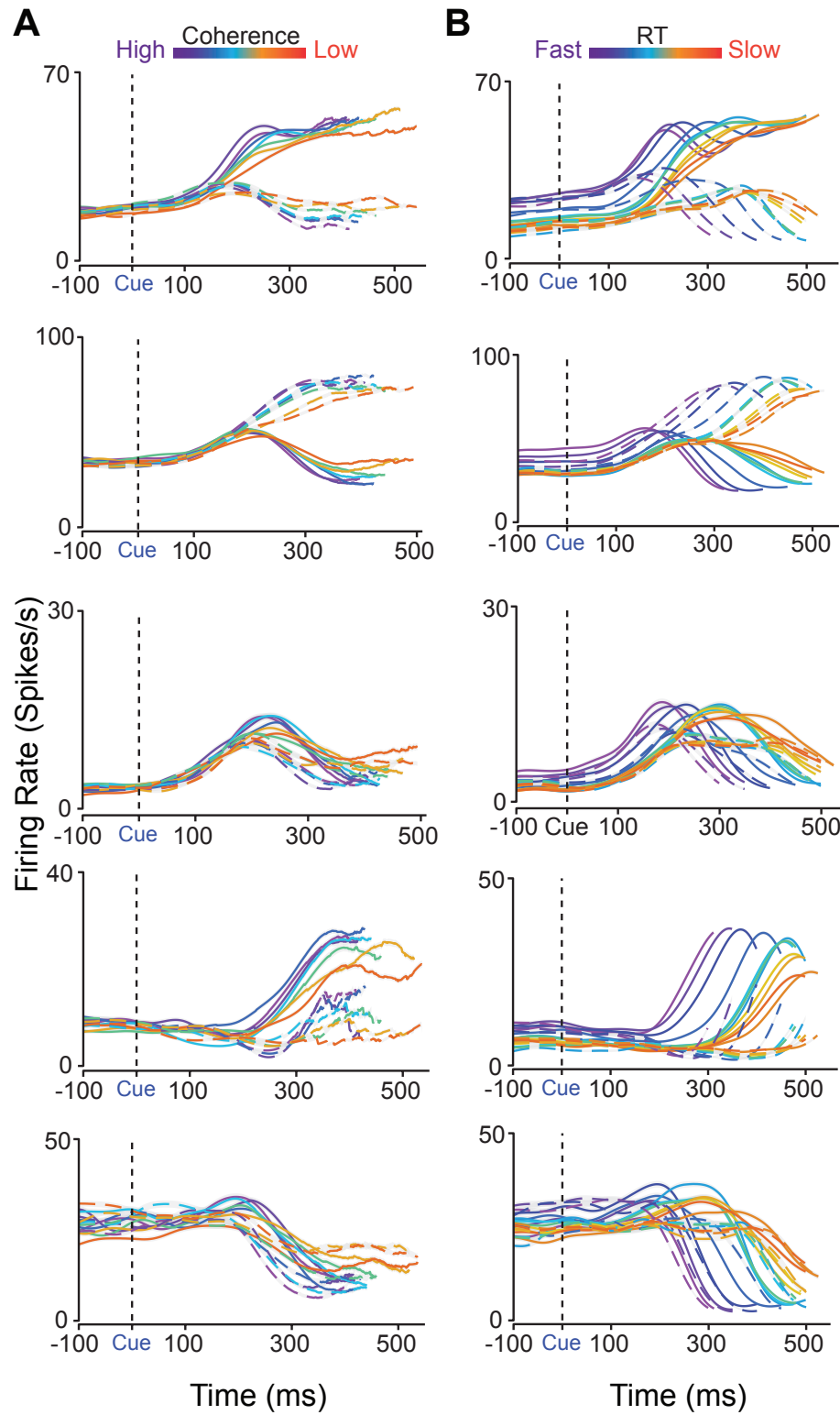


Figure 3: Firing rates of a heterogeneous population of PMd neurons modulate their firing rates as a function of RT before stimulus onset (A, B) Firing rate activity across (A) 7 levels of color coherence and (B) 11 RT bins and both reach directions (right - dashed, left - solid) of 6 example single units in PMd from monkeys T and O aligned to stimulus onset (**Cue**/vertical dashed black line). Firing rates are plotted until the median RT of each color coherence and until the midpoint of each RT bin (notice slightly different lengths of lines). The gradation of color indicates either the level of difficulty for the coherence (purple - mostly one color, red - nearly even split of red and green squares) or RT speed. Gray outlines visible around some lines represent $2 \times SEM$.

Trajectories for fast RTs are also more in plane with the movement initiation point compared to slower RTs, and slower RTs appear to involve a longer excursion from the starting point to the movement initiation state. In contrast, there appears to be little to no separation by choice. Such variation in prestimulus neural state, and covariation between prestimulus neural state and RT was observed even within a level of stimulus coherence (compare Fig 4B & Fig 4B, inset).

Collectively, our visualization using PCA suggest a representational geometry for decision-making in RT tasks where prestimulus state predicts post-stimulus dynamics and covaries with RT but not the eventual choice. In subsequent sections, we use a wide variety of analysis to understand this representational geometry through the lens of the initial condition hypothesis.

2.4. Slower RTs are accompanied by slower pre- and post-stimulus dynamics, and necessitate larger changes in firing rates

The first prediction of the initial condition hypothesis is that the initial conditions predicts the speed and location of the post-stimulus dynamics.

We first used the recently developed Kinematic analysis of Neural Trajectories (KiNeT) approach to quantify the structure in these trajectories (Remington et al., 2018). KiNeT compares trajectories to a reference trajectory and measures speed and spatial location with respect to this reference trajectory. For measuring speed, KiNet marches along a reference trajectory and identifies for every other trajectory the timepoint with the minimal euclidean distance to the timepoint in reference trajectory. Trajectories slower than the reference trajectory will only reach the point on the reference trajectory later in time, whereas trajectories faster than the reference trajectory will reach the point on the reference trajectory earlier. KiNet also reports the signed minimum euclidean distance at each point for the trajectory, which reports how the trajectory is organized relative to the reference trajectory. KiNeT revealed that faster RTs involved faster pre- and post-stimulus dynamics whereas slower RTs involved slower dynamics as compared to a reference trajectory (trajectory associated with middle RT bin, cyan) (Fig 4C, top). Trajectories were also found to be spatially organized by RT (Fig 4C, bottom) with fast and slow RT trials organized relative to the reference RT trajectory.

Two other analyses allowed us to further quantify the geometrical structure of these state space trajectories. First, the speed of the prestimulus state in the first six dimensions covaried with RT. Second, the excursion from prestimulus state to movement initiation as measured by the high-dimensional euclidean distance between the prestimulus state and the premovement state was smaller for faster compared to slower RTs. We also examined if prestimulus state covaried with choice. The euclidean distance on a timepoint by timepoint basis between left and right choice trajectories was largely flat before stimulus onset and increased only after stimulus onset.

2.5. Prestimulus spiking activity explains RT variability but does not predict eventual choice

RT variability could be caused by differences in the speed and/or starting point of the neural dynamics. However the PCA results were performed on trial-averaged firing rates which can obscure different causes of RT variability. To better understand how decision-related dynamics evolve on single trials, we performed a single-trial analysis on simultaneously collected neural data from PMd. We used Latent Factor Analysis of Dynamical Systems (LFADS) (Pandarinath et al., 2018) to visualize single trial dynamics. The analysis (Fig 5A) reveals that although, some of the initial states for slow RTs are also mixed in with fast RTs, many of the single trial trajectories for fast and slow RTs differentiate in neural state space 200 ms before stimulus onset. Consistent with our PCA results, initial neural states related to left and right reach are mixed prior to stimulus onset (Fig 5E). These results further bolster the notion that prestimulus spiking activity covaries with RTs but not choice, even on single trials.

Regression analyses confirmed the insights from visualization. Pre-stimulus spiking activity explained ~25% of the variance in RT in the single session (Fig 5B) and ~15% of the variance on average across all sessions (Fig 5C). This variance was significantly higher than the 99th percentile of trial shuffled spiking activity regressed with RT for the single session (Fig 5B) and across all sessions (Fig 5D). In contrast, prestimulus spiking activity failed to predict choice above chance levels and was no better than the 99th percentile of the trial shuffled spiking

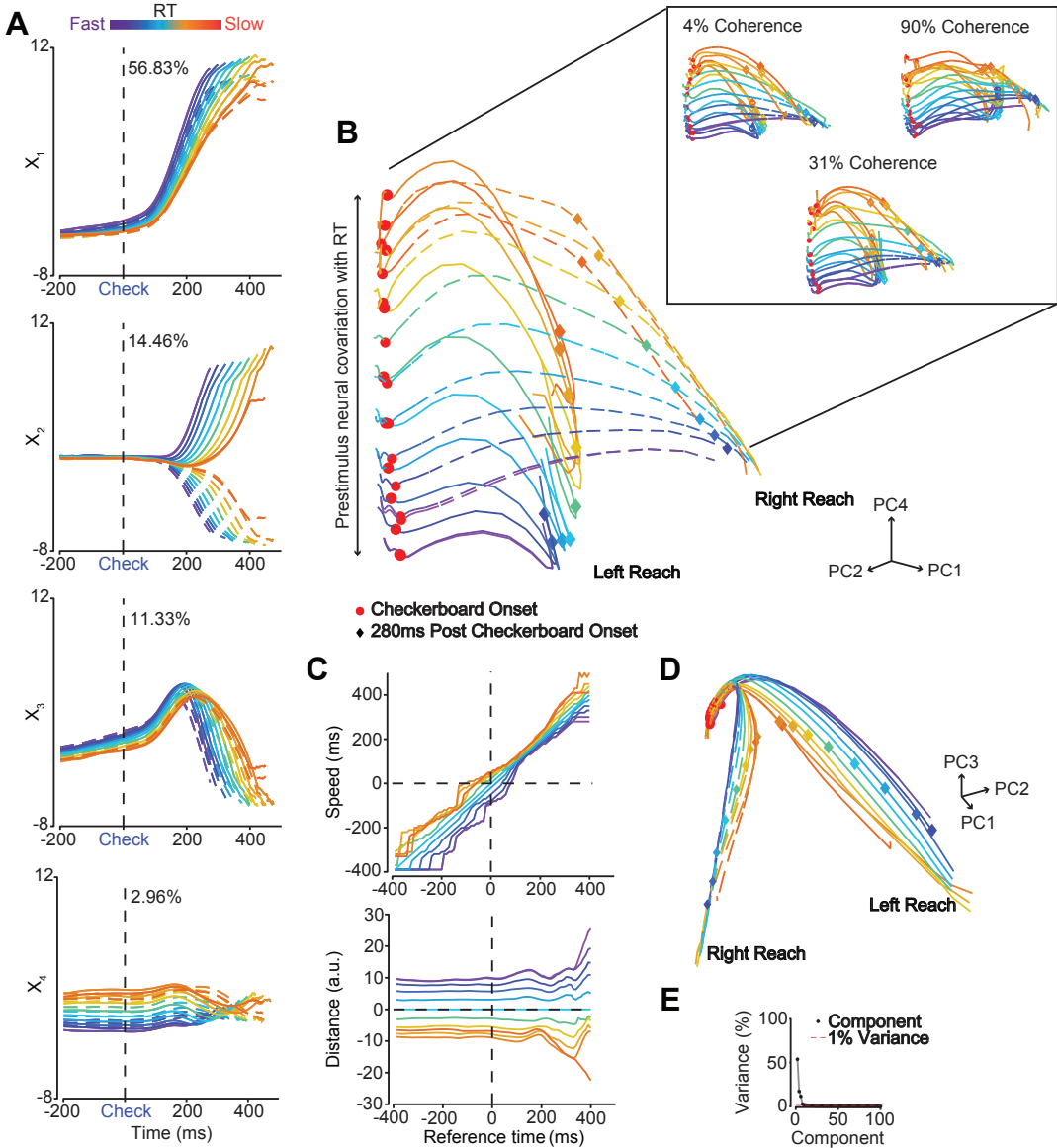


Figure 4: Prestimulus population firing rates covary with RT (A) The first 4 PCs ($PC_{1,2,3,4}$) of trial averaged firing rates of all 996 neurons from both monkeys and all sessions organized across 11 RT bins (purple - fastest bin to red - slowest bin, both reach directions (right - dashed lines, left - solid lines), and aligned to checkerboard onset ('Check' & black dashed line). Percentage variance explained by each PC presented at the top of each plot. (B) State space of the 1st, 2nd and 4th PCs ($PC_{1,2,4}$) aligned to checkerboard onset (red dots). Different colored diamonds indicate 280 ms post-checkerboard onset. Notice that the plotting of PCs extends 200 ms before stimulus onset. Inset: 3D state space of the 1st, 2nd and 4th PCs for a subset of the seven PCAs conditioned on RT bins and reach performed within a single stimulus coherence (4%, 31%, & 90%). (C) "KiNeT" speed (top) and distance (bottom) analyses respectively showing that pre- and post-stimulus speed is faster for faster RTs as compared to a reference trajectory (cyan, middle trajectory) and that trajectories are spatially organized by reference time. Abbreviation: a.u. - arbitrary units. (D) 3D structure of the first 3 PCs ($PC_{1,2,3}$) aligned to checkerboard onset (red dots). Remark how neural activity separates as a function of choice and coherence < 200 ms post-stimulus onset (similar structure to SFig 1B). (E) Scree plot of the percentage of variance explained by the first 50 components. The first 4 PCs capture $> 85\%$ of the variance in the firing rate activity.

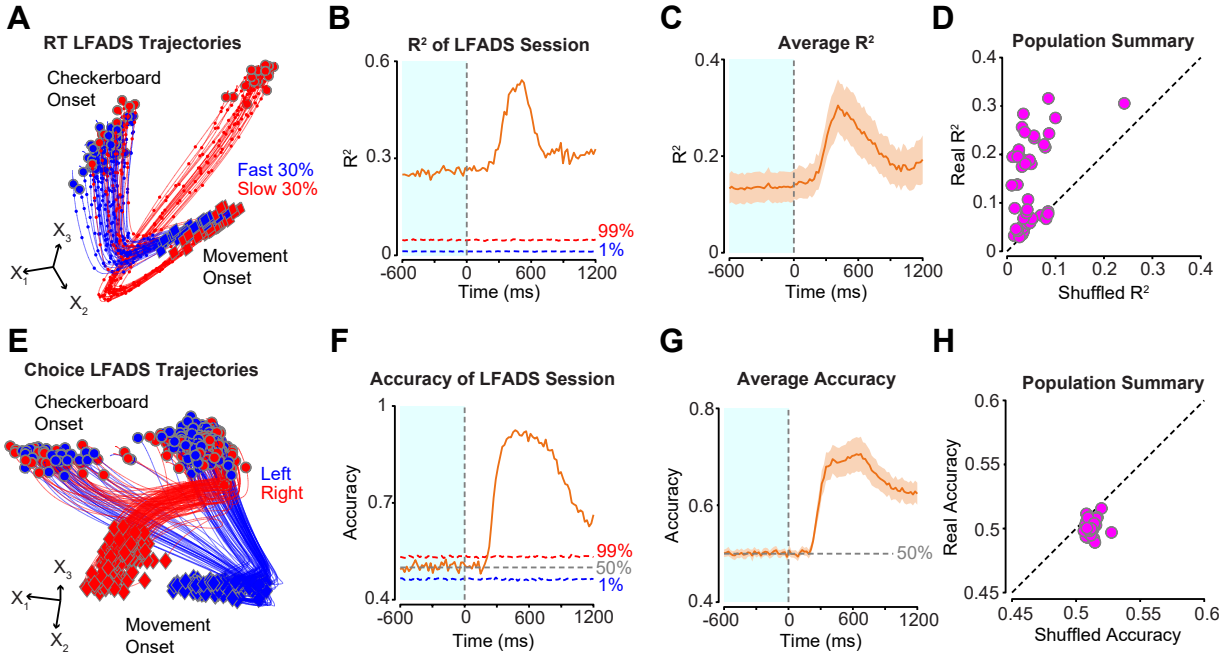


Figure 5: Single trial analysis, linear regression, and decoders reveal that neural activity differs as a function of RT but not choice prior to stimulus onset (A & E) LFADS (Pandarinath et al., 2018) trajectory through the state space of the first 3 latent factors $X_{1,2,3}$ plotted for **A** the fastest 30% of trials (blue) and the slowest 30% of trials (red) and **E** for left (blue) and right (red) reaches within the easiest coherence from a single session. Each trajectory is plotted from 200 ms before checkerboard onset to movement onset (red/blue dots and diamonds respectively). Small dots in the trajectories are the position of the first 3 latent factors every 50 ms. (**B/F**) Plot of variance explained R^2 /accuracy from linear/logistic regressions of binned spiking activity (20 ms) to predict trial-matched RTs/eventual choice from all 23 neurons in the LFADS session. The blue and red dotted lines represent the 1st and 99th percentiles of R^2 /accuracy values calculated from averaged models of trial-shuffled spiking activity and RTs/choice (shuffled 500 times). The grey dotted line in (F) represents 50% accuracy. (**C/G**) Plot of R^2 values, calculated as in (B/F), averaged across 51 sessions. Orange shaded area is the 99% confidence interval of the mean ($2.58 \times SEM$). The grey dotted line in (G) represents 50% accuracy. (**D/H**) Scatterplot of true prestimulus R^2 /accuracy values compared to the R^2 /accuracy value for the 99th percentile of the shuffled data. Each dot represents the bin- and trial-averaged prestimulus R^2 /accuracy value within each of the 51 sessions. Dotted line is where scatter points would fall if shuffled R^2 and real R^2 values were equivalent. (**D**) Many of the points lie above this line suggesting that real prestimulus neural activity explains more of the RT variance than shuffled neural data. (**H**) In contrast, many of the points lie on or below this line suggesting that real prestimulus neural activity is not predictive of choice.

activity either in a single session (Fig 5F) or across all sessions (Fig 5G & H). Even when trials were grouped by RT bins (Fig ref), we were unable to use the prestimulus spiking activity to predict eventual choice better than chance levels. These results are consistent with the initial condition hypothesis and the idea that prestimulus activity covaries with RT but not choice. Such a finding further bolsters our hypothesis that prestimulus state predict post-stimulus dynamics and eventual decision-making behavior.

2.6. The outcome of the previous trial influences prestimulus spiking activity

Thus far we have demonstrated that prestimulus population spiking activity largely explains RT variability in a decision-making task. However what contributes to the trial-by-trial prestimulus neural population variation remains unclear. One source of prestimulus neural variation could be post-error adjustment which is a behavioral phenomenon where RTs for trials following an error are typically slower and sometimes faster than RTs in trials following a correct response (Danielmeier and Ullsperger, 2011). Given that post-error adjustment can contribute to RT variability, we expect this variability to be accompanied by shifts in trial-to-trial neural state. We set out to find evidence that neural population state differs after an error as compared to a correct response, leading to slower pre- and then post-stimulus dynamics and that may contribute to slower responses after an error.

A behavioral analysis confirmed that post-error adjustment occurred across both subjects. All trial sequences of correct, error, correct and their associated RTs were aggregated across both monkeys and all sessions. All sequences with a RT < 200 ms were removed from the analysis (0.3% of trials). Correct trials following an error were significantly slower than correct trials immediately preceding the error trial ($M \pm SD: 468 \pm 118$ ms, 449 ± 105 ms; Wilcoxon rank sum comparing median RTs, $p = 4.99e-97$) (Fig 6D).

To assess whether errors led to a shift in the prestimulus neural state in the following trial we performed a principal component analysis (PCA) on all 996 units and their trial-averaged firing rate activity windowed about checkerboard onset and conditioned on previous trial outcome and choice (Fig 6A & B). Expectedly, the PCA revealed similar decision-related PCs as previously observed, with the first PC (50.16%) representing a change in firing rates after stimulus onset and the second (13.94%) and third (11.96%) PCs showing a mix of firing rate changes and choice behavior post-stimulus (Fig 6A, top three panels). In the 4th PC (2.28%), a considerable separation in population neural dynamics occurs before stimulus onset and endures at least 400 ms past checkerboard onset between post-error and all other trial types for both reaches (Fig 6A, 4th panel & Fig 6B). Similarly, a decoder revealed that current trial spiking activity can predict the previous trial's outcome from before stimulus onset until about the overall mean response time, ~ 500 ms after checkerboard onset, at higher than chance levels (Fig 6C). Furthermore a KiNeT analysis revealed that pre-stimulus, post-error population dynamics differed in state space and had slower prestimulus trajectories as compared to all other trial types (Fig 6X). These findings are consistent with the initial condition hypothesis as they demonstrate that prestimulus population neural activity is dependent upon trial history and that prestimulus dynamics slow down after errors as compared to after correct trials, providing a powerful explanation for slower RTs after errors.

2.7. Behavioral models that include a gain signal outperform standard DDMs

One candidate mechanism that could act as a neural level mechanism for altering population neural state would be a stimulus-independent, variable gain signal, often termed 'urgency' (Cisek et al., 2009). Trial-history dependent prestimulus neural activity covaries with and is explanatory of RT but does not predict choice, consistent with a variable stimulus-independent gain signal. Therefore models of decision-making that include an 'urgency' signal should theoretically outperform models without urgency, further corroborating our findings. To this end we employed a behavioral modeling toolbox that we recently developed (Chandrasekaran and Hawkins, 2019), which allows for the selection and rigorous fitting of various behavioral models.

Two major groups of cognitive process models, standard drift diffusion models (DDMs, Ratcliff 1978) and urgency DDMs, were built to test out ideas of decision-making (Fig 7A:D). The $DDMS_vS_zS_t$ with a variable drift rate (S_v), variable start point (S_z), variable non-decision time (S_t) and 2 bounds (A & 0) (Fig 7A) greatly overestimates the 90th percentile of the RT distribution of most coherences for both monkeys (Fig 7E, top and bottom panels). Other non-urgency DDM variants have a zero or nearly non-negative AIC score (Fig 7F, top and bottom panels). As time increases in a collapsing (c) bounds ($A(t)$ & $a - A(t)$) DDM less evidence is needed to cross a boundary and therefore make a choice (Fig 7B). $cDDMS_vS_z$ slightly overestimates the 90th percentile of the RT distribution for the hardest coherences for monkey T (Fig 7E & F, top panels), but is the best model for describing the RT distributions in monkey O (Fig 7E & F, bottom panels). Finally in the last two models, an urgency (u) DDM ($uDDMS_bS_u$) (Fig 7C) and a nonlinear urgency (nlu) DMM ($nluDDMS_bS_u$) (Fig 7D), the drift rate is scaled by a linear and nonlinear gain term respectively such that as time elapses the gain signal grows and pushes the drift rate closer to a bound with relatively less evidence. Both of these models perform very well for both monkeys with RT distributions being captured well across all levels of coherence and large negative AIC scores (Fig 7E & F).

Overall models with a variable gain term or 'urgency' were substantially better at describing the behavior of the monkeys than models without urgency (e.g. compare $uDDM$ to DDM) (Fig 7F). Moreover, models with variable gain signals were even better than models without variability (e.g. compare $uDDMS_bS_u$ to $uDDM$) (Fig 7E, F). Together, the observations from behavioral modeling lend credence to the suggestion that a variable, stimulus-independent gain signal alters decision-related dynamics and could potentially serve as a neural mechanism for altering prestimulus population dynamics.

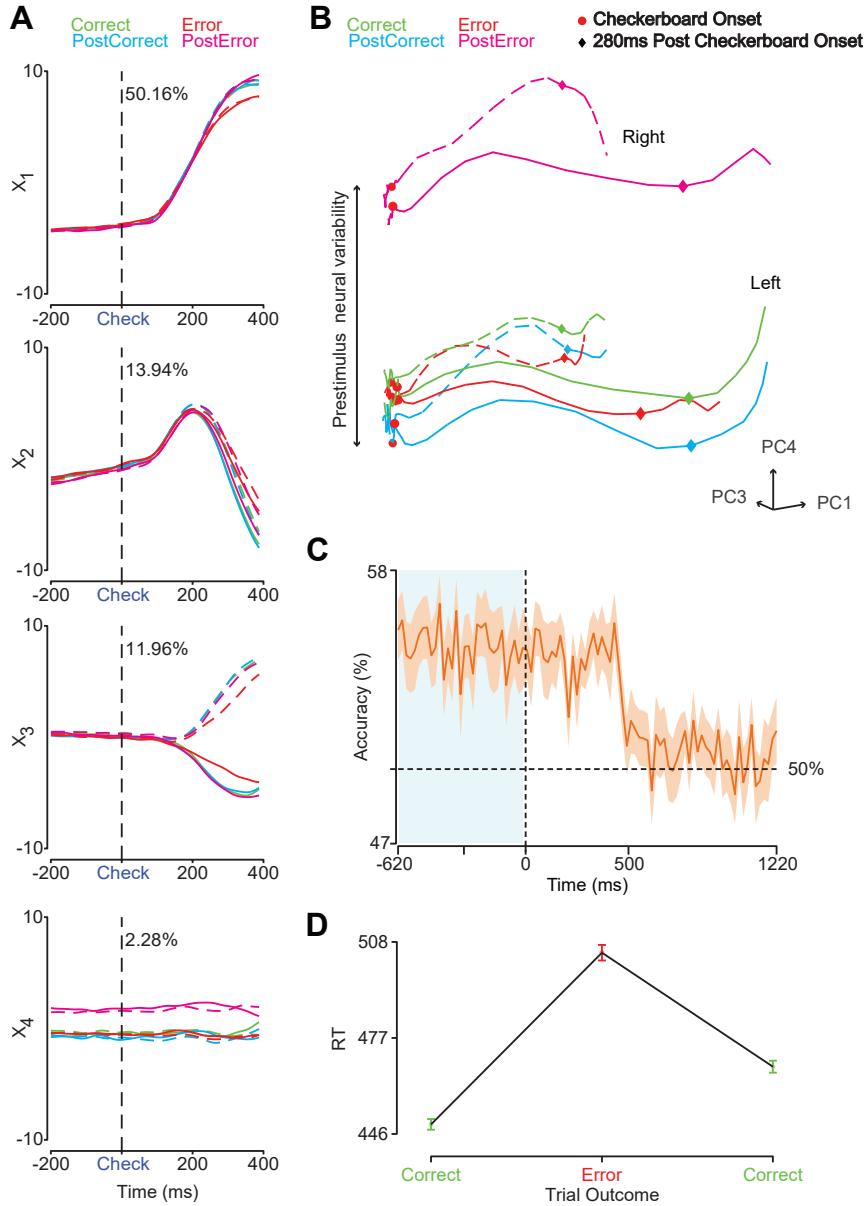


Figure 6: Prestimulus neural activity covaries with the previous trial's outcome **(A)** The first 4 PCs ($PC_{1,2,3,4}$) of trial averaged firing rates aligned to checkerboard onset ('Check' & black dashed line) of all 996 neurons from monkeys T & O and all sessions organized by choice (right - dashed lines, left - solid lines) and trial outcome (green - correct trial, cyan - correct trial following a correct trial, red - error trial, and magenta - trial following an error trial). Percentage variance explained by each PC presented at the top of each plot. **(B)** 1st, 3rd and 4th PC ($PC_{1,3,4}$) state space aligned to checkerboard onset (red dots). Plotting of PCs extends 200 ms before checkerboard onset and 400 ms after. Observe how neural activity separates as a function of outcome, but not by choice, up to 200 ms before stimulus onset. Different colored diamonds indicate 280 ms post-checkerboard onset. **(C)** Accuracy of logistic regression of spiking activity from the current trial used to predict the outcome of the previous trial. Orange outline is the 99% confidence interval. **(D)** Average RTs from all correct, error, correct sequences found across both monkeys and all sessions. Error bars are $2 \times SEM$.

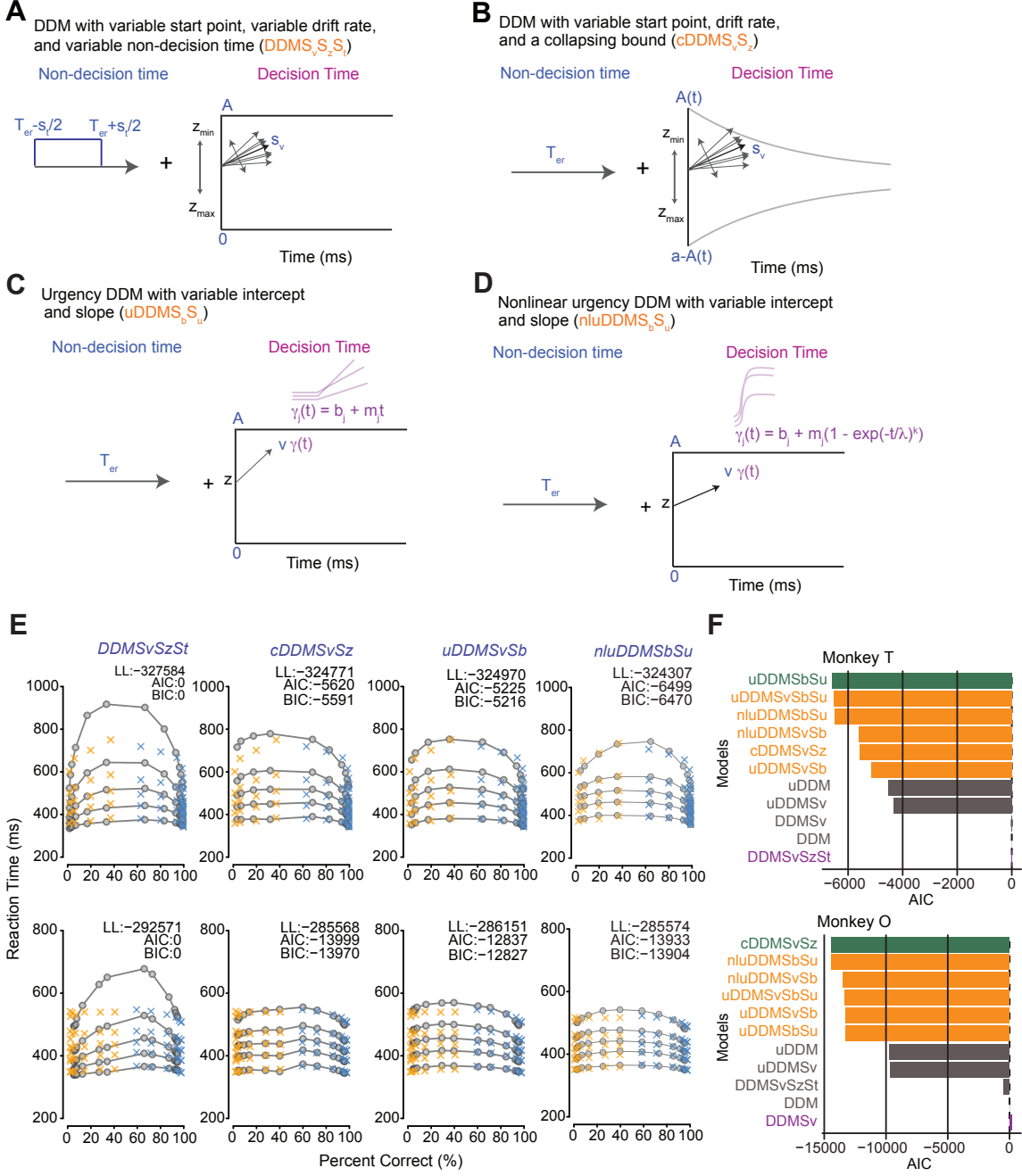


Figure 7: Behavioral outcomes are best predicted by models that include urgency (A) Drift diffusion model (DDM), models decision-making with variable non-decision time (S_t), a variable start point (S_z), variable drift rate (S_v) and fixed bounds (A & 0). (B) DDM with fixed non-decision time (T_{er}), variable starting point (S_z), variable drift rate (S_v), and collapsing (c) bounds ($A(t)$ & $a - A(t)$). (C) Urgency (u) DDM with fixed non-decision time (T_{er}), a fixed drift rate (v), multiplicative urgency term ($\gamma(t)$), and fixed bounds (A & 0). The urgency term has a variable intercept (S_b) and slope (S_u), and acts as a gain on the drift rate. (D) Nonlinear urgency (nlu) DDM with fixed non-decision time (T_{er}), fixed drift rate (v), multiplicative urgency term ($\gamma(t)$), and fixed bounds (A & 0). Here the urgency model has a variable intercept (S_b) and variable slope (S_u) scaled by a nonlinear sigmoidal function. (E) Quantile probability plots of 4 decision-making models for monkeys T (top row) & O (bottom row). The grey circles (model predictions for accuracy and RT distributions) and x's (behavioral data) are plotted for the 10th, 30th, 50th, 70th, and 90th percentile of the RT distribution. Columns of blue x's are the proportion correct for each coherence, whereas columns of yellow x's are the proportion of errors for that coherence. LL - Log Likelihood, AIC - Akaike Information Criterion, BIC - Bayesian Information Criterion. (F) AIC scores for all tested models for both monkeys. The lower the AIC score the better the model is at predicting behavior. Models are listed in increasing order of AIC score (i.e. they become less negative).

3. Discussion

3.1. Summary

Our goal in this study was to better understand the neural population dynamics underlying decision-making in RT tasks and to rigorously investigate if the dynamics are consistent with the initial condition hypotheses recently identified in studies of motor planning and timing (Afshar et al., 2011; Remington et al., 2018). To this end, we investigated the population dynamics recorded from PMd neurons of monkeys performing a red-green RT decision-making task. Prestimulus neural state was strongly predictive of RT, but not choice across and within stimulus difficulties, with similar dynamics observed on individual trials. Furthermore, faster RT trials had faster neural dynamics, separate initial neural states, and shorter overall trajectories than slower RT trials. These results are all consistent with an initial condition hypothesis that parameterizes action timing, but not action choice. Additionally, prestimulus population dynamics were found to change as a result of the previous trial's outcome, where RTs and prestimulus trajectories were generally slower for post-error trials than post-correct trials. Finally, cognitive process models that assumed a gain signal were the superior predictors of decision-making behavior. Together, these results are consistent with the initial condition hypothesis and suggest that a variable gain signal modifies prestimulus population dynamics in a trial-history dependent manner leading to faster or slower reaction times. In the remainder of the discussion, we further discuss the generalizability of these results and what may be driving initial conditions.

3.2. Initial condition hypothesis as a general brain dynamic

Studies of decision- and choice-related neural activity throughout animal models suggest that evolutionarily conserved, generalized brain dynamics which primarily subserve motor activity and motor planning, are also likely the basis for decision-making (Roitman and Shadlen, 2002; Hanks and Summerfield, 2017; Briggman et al., 2005; Bahl and Engert, 2020; Groschner et al., 2018; Cisek, 2012; Zagha et al., 2022). In motor planning research the neural state at the go cue was the best predictor of RTs, explaining more variance in RTs than other tested models (Afshar et al., 2011) and potentially more than 50% of movement variability (Churchland et al., 2006a). Additionally, in timing studies, where animals must reproduce an observed time interval, again the speed and position of initial conditions at a go cue largely determine when the animal produces a behavioral response (Remington et al., 2018). These results are further generalized and corroborated by findings in place cell research where the strongest predictor of a rat's eventual choice to enter the left or right arm of a maze was the initial population state during a delay period (Pastalkova et al., 2008). These three, broadly speaking motor planning studies with a delay, suggest that for motor behavior in well learned tasks, population dynamics evolve adhering to trajectories as defined by initial conditions at a go cue.

Findings of prestimulus shifts in neural activity in studies of SAT (Murphy et al., 2016; Heitz and Schall, 2012; Hanks et al., 2014; Bogacz et al., 2010) and post-error adjustment (Thura et al., 2017; Purcell and Kiani, 2016; van den Brink et al., 2014) hint that this mechanism may generalize to more complex behavioral paradigms that involve making a choice according to environmental evidence such as in perceptual decision-making. Indeed, our results suggest that this is the case. While we did not directly manipulate SAT we do observe considerable covariation between prestimulus population state and RTs, even within a stimulus difficulty, and the covariation captures more variance than the level of stimulus difficulty itself. Similarly we demonstrate that population activity separates as a function of previous trial outcome prior to stimulus onset and this change in activity is associated with slower RTs. Finally, these prestimulus shifts in population state are reminiscent of prestimulus differences in neural activity between task instructions of responding accurately or quickly and post-error adjustment. We speculate that this prestimulus shift in neural activity observed in SAT and post-error adjustment rely upon the same mechanism, namely a difference in initial conditions in population state that either speeds up or slows down the response of the actor (Danielmeier and Ullsperger, 2011). Theoretically, error feedback or instructions to prioritize accuracy/speed, modulates the initial population state, either via a gain signal or through recurrent activity, such that it is closer or further from a motor initialization state in order to possibly modulate the evidence accumulation process.

3.3. Decision-making as motor planning, and relation to general dynamics

Originally considered as a contaminant of task-related signals, motor signals are now considered to explain the largest swath of variance in neural activity (Zagha et al., 2022). There is recent widespread consensus across animal models that the brain generally evolved to process motor signals (cite rodent literature and Cisek). Furthermore theoretical work posits essentially that higher 'cognitive' functions such as perceptual decision-making are essentially processed in the brain as motor plans (cite Cisek). Tantalizingly, motor planning research, theorized as part of the decision-making process, demonstrates that a majority of variability in reaction times (RTs) is explained by neural activity prior to the go-cue rather than any neural variability during motion [32, 33, 34]. This is consistent with urgency and multiple motor plan hypotheses in that decision-making relies on motor planning. Additionally, RTs are known to vary as a function of trial history [35] and trial-to-trial alterations in RT are accompanied by changes in prestimulus neural activity [8, 32, 7, 28, 29].

Studies of decision-related neural activity throughout animal models suggest evolutionary conserved neural mechanisms of decision-making Roitman and Shadlen (2002); Hanks and Summerfield (2017); Briggman et al. (2005); Bahl and Engert (2020); Groschner et al. (2018).

3.4. Trial-history dependent global fluctuations contribution to trial-to-trial behavioral and subpopulation variability

In this study we find behavioral and electrophysiological evidence for post-error adjustment ([in this case slowing for both monkeys \(supplementary\)](#)). That is after an error is made prestimulus population dynamics are slower and the monkeys are slower to respond as compared to after a correct response. Post-error adjustment is a reliable individual trait, however adjustments rarely precede an improvement in performance ([Danielmeier and Ullsperger, 2011](#)); [corroborated in this study with nearly overlapping post-correct and post-error trial psychometric curves \(supplementary\)](#). Therefore what is achieved by post-error adjustment remains unclear. A prominent hypothesis is that post-error adjustment is a reorientation of task engagement due to an unexpected event ([Danielmeier and Ullsperger, 2011](#); [van den Brink et al., 2014](#)). With enough time between trials post-error adjustment is no longer observed ([Danielmeier and Ullsperger, 2011](#)), suggesting, speculatively, that a transition between behavioral states or global fluctuations may be complete ([van den Brink et al., 2014](#)).

Task engagement is reported to be indexable by low frequency global oscillations as found across species (e.g., humans, monkeys, and mice: ([van den Brink et al., 2014](#); [Lakatos et al., 2008](#); [Jacobs et al., 2020](#))). Low frequency global oscillations (e.g., delta oscillations) are found to entrain to the frequency of stimulus presentation such that the phase of the brain oscillation at the time of stimulus onset is predictive of response latency ([Lakatos et al., 2008](#); [van den Brink et al., 2014](#)). Similar evidence in mice suggest that low frequency oscillations (i.e. 3 - 6 Hz; 'mouse alpha') are also indicative of task engagement ([Jacobs et al., 2020](#)). The amount of 3-6Hz global desynchronization, especially over somatosensory cortex, prior to stimulus onset is predictive of response latency and whether an action will be made, but is not predictive of perceptual accuracy. That is the more desynchronized the frequency band the faster the RT and the more likely a choice will be made at all, but not whether it will be correct or incorrect ([Jacobs et al., 2020](#)). Furthermore, after an error trial, the prestimulus low frequency oscillations are generally more out of phase with the frequency of presented stimuli than after a correct trial. And the less in phase they are, the greater the effect of post-error slowing ([van den Brink et al., 2014](#)). These results further buttress the initial condition hypothesis across species, tasks, and brain areas suggesting that initial conditions from a dynamical systems perspective are generally predictive of the latency of a behavioral response regardless of context. They also suggest that initial conditions in a brain area are affected by global brain activity, likely indicative of the animal's general behavioral state, which may act as a gain signal on recurrent dynamics in sub-populations, altogether affecting response latency. Lastly the weight and ubiquity of evidence suggests this is a principled/generalized brain dynamic, explanatory and predictive of subsequent brain dynamics at multiple spatial/time scales and behavior, regardless of context.

3.5. Gain signals contribute to trial-to-trial neural variability and therefore initial conditions

Fundamentally we are trying to discern between two possible models of brain activity, one that is gain modulated and one that is not. As an illustration, it is possible that neural processes related to post-error adjustment either

directly affect initial conditions in PMd or an external gain signal interacts with initial conditions in PMd to drive behavior. More concretely we present four possible ways in which gain signals may or may not interact with dynamic population activity.

$$\frac{dx}{dt} = f(x(t)) + U(t) \quad (1)$$

$$\frac{dx}{dt} = f(x(t)) + U(t)g(t) \quad (2)$$

$$\frac{dx}{dt} = f(x(t), g(t)) + U(t) \quad (3)$$

$$\frac{dx}{dt} = f(x(t), g(t)) + U(t)g(t) \quad (4)$$

The future state of the system ($\frac{dx}{dt}$) is determined by the current firing rates of the observed neurons ($f(x(t))$), their initial conditions (x_0), and modified by a constant or context/time dependent external input (U) (e.g. other neural populations). The external input or recurrent population dynamics could be gain modulated ($g(t)$). Equation (1) is a simple dynamical system which is a function of its current state and an external input, equations (2) and (3) include a gain signal either on the external input or current state respectively, and in equation (4) there's a shared gain signal on the current state and the external input. More complex models that include more gain signals or that multiplex gain signals could be imagined, however the drive was to model a dynamical system with relatively few parameters. Furthermore studies where gain signals were modeled to contribute to trial-to-trial neural variability revealed that relatively few gain signals (e.g. 4) were needed to recapitulate observed population activity, with just a couple of gain signals (e.g. 1-2) needed to capture a majority of the variance (Stroud et al., 2018; Rabinowitz et al., 2015; Goris et al., 2014). While our PMd data cannot distinguish between these possibilities, we have designed several models to distinguish between gain or no gain models .

We have demonstrated that initial dynamics change on a trial-by-trial basis and that cognitive process models that included a gain term or time sensitive bounds best described our behavioral data. Additionally, in our supplementary materials, RNN modeling that included a variable, tonic multiplicative or additive gain signal best recapitulated our pre- and post-stimulus PMd population dynamics as compared to a model with no such gain term. A large body of neurophysiological evidence and modeling suggests that numerous populations of neurons throughout the brain demonstrate trial-to-trial variation attributable to multiplicative or additive gain signals (Ferguson and Cardin, 2020; Murty and Arun, 2018; Williams and Linderman, 2021; Cisek et al., 2009; Goris et al., 2014). Our findings and those of others (Remington et al., 2018; Goris et al., 2014; Rabinowitz et al., 2015) point to a stimulus-independent tonic/slowly varying gain signal which modulates initial conditions on a trial-to-trial basis and drives post-stimulus neural dynamics and behavior. Results from our study support the model in which a shared gain signal variably modulates the prestimulus population dynamics as well as the gain on the stimulus input (i.e. 'urgency' or 'impulsiveness') (Cisek et al., 2009).

3.6. Initial condition hypothesis as a general brain dynamic and computation via dynamics

Furthermore the weight and ubiquity of evidence suggests this as a principled/generalized brain dynamic, explanatory and predictive of subsequent brain dynamics and behavior at multiple scales and regardless of context. As future behavior of dynamical systems are known to heavily rely upon initial conditions and given that we observe the importance of initial conditions in many contexts, as well as increased explanatory and predictive power when examining the brain as a dynamical system highly suggests that the brain at multiple scales performs its computations as a dynamical system. At this point it is very likely that the brain computes via dynamics, 'Theory of computation via dynamics'. The brain at multiple scales, time scales, different brain areas, sensory

modalities, species, it is clear that initial conditions are predictive of subsequent brain dynamics, response latency, movement kinematics and whether there is behavioral response at all. Moreover initial conditions explain why we are able to predict RT from prestimulus activity in a more informative way than before. Before we look at the synchronization or desynchronization of neurons, so if you are more desynchronized you respond faster but why? With ICH we have a principaled way of explaining it, either trajectory is further, slower or both. We have also shown the importance of gain signals in this task and as is seen across studies and again across many levels of brain activity. We and many other studies also show that the future state of the PMd is a function of its latent variables, its current state, and external inputs into the system. Satisfying the conditions for a dynamical system. Beyond this we must discuss the representational view of neuroscience (Shenoy et al., 2013). Indeed one of the things that this perspective suggests, and as I think is widely becoming understood, is that trial-averaging of brain activity, while productive, is flawed. We should be moving more towards single trial analyses and working on methods to improve single trial analysis and finding similarity between trials rather than mushing them altogether.

3.7. Unresolved questions, future directions and caveats

Do we see hints of ICH in more cognitive contexts, i.e. in brain processes/contexts that do not that require a motor output? Perhaps a corollary could be observed in resting state dynamics.

Now to expand or generalize further. So far we have seen that initial population dynamics can be used to predict choice (Pastalkova et al., 2008), predict RTs in decision-making and motor planning (Afshar et al., 2011), and determine the timing of a behavioral response (Remington et al., 2018). All of these are instructed tasks. What about for voluntary movements? Does the initial condition hypothesis extend to voluntary movements and beyond that to internal dynamics, ie dynamics that do not produce a behavioral output (e.g. thought or visualization) or perhaps an intention to make a movement. This harks back to Libet 1983 that conscious decisions are pre-ordained by a motor preparation signal, readiness potential. Suggesting the role for initial conditions prime conscious, voluntary decisions and therefore could play a role in most types if not all types of cognitive and purely motor signals. There's evidence that preparatory activity precedes voluntary and instructed behavioral responses from simple motor planning to more cognitively challenging tasks such as perceptual decision-making. If a behavioral response is not required for some internal state do we still see strong contributions from initial conditions? Evidence suggests that even with non-instructed or more self-initiated type movements that initial conditions predict the timing and the movement kinematics (Lara et al., 2018).

3.8. Conclusions

Furthermore dynamical systems/computation-by-dynamics/representational geometry (Kriegeskorte and Kievit, 2013) offer a parsimonious explanation for such trial-to-trial variability in that individual neuron variability can be high but what is revealed in population state space are stereotyped patterns of activity that represent the stimuli and lead to similar outputs (Williams and Linderman, 2021; Shenoy et al., 2013).

Studies of decision- and choice-related neural activity throughout animal models suggest that evolutionarily conserved, generalized brain dynamics which primarily subserve motor activity and motor planning, are also likely the basis for decision-making (Roitman and Shadlen, 2002; Hanks and Summerfield, 2017; Briggman et al., 2005; Bahl and Engert, 2020; Groschner et al., 2018; Cisek, 2012; Zagha et al., 2022).

4. Methods

Several method sections are adapted from Chandrasekaran and others 2017 (Chandrasekaran et al., 2017) as the same data set is reanalyzed in this study.

4.1. Code and data availability

MATLAB live scripts for generating all the figures are available with the paper along with the relevant data. HTML code that allows free rotation of the trajectories in principal component spaces are also available in the Zip file.

4.2. Subjects

Experiments were performed using two adult male macaque monkeys (*Macaca Mulatta*; monkey T, 7 years, 14 kg & monkey O, 11 years, 15.5 kg) trained to touch visual targets for a juice reward. Monkeys were housed in a social vivarium with a normal day/night cycle. Protocols for the experiment were approved by the Stanford University Institutional Animal Care and Use Committee. Animals were initially trained to come out of their housing and to sit comfortably in a chair. After initial training (as described in ([Chandrasekaran et al., 2017](#))), monkeys underwent sterile surgery where cylindrical head restraint holders (Crist Instrument Co., Inc., Hagerstown, MD, United States) and standard recording cylinders (Crist Instrument Co., Inc.) were implanted. Cylinders were placed surface normal to the cortex and were centered over caudal dorsal premotor cortex (PMdc) (+16, 15 stereotaxic coordinates). The skull within the cylinder was covered with a thin layer of dental acrylic.

4.3. Apparatus

Monkeys sat in a customized chair (Synder Chair System, Crist Instrument Co., Inc.) with their head restrained. The arm that was not used to respond in the task was gently restrained with a tube and cloth sling. Experiments were controlled and data collected using a custom computer control system (Mathworks' xPC target and Psychophysics Toolbox, The Mathworks, Inc., Natick, MA, United States). Stimuli were displayed on an Acer HN2741 monitor approximately 30 cm from the monkey. A photodetector (Thorlabs PD360A, Thorlabs, Inc., Newton, NJ, United States) was used to record the onset of the visual stimulus at a 1 ms resolution. A small reflective spherical bead (11.5 mm, NDI passive spheres, Northern Digital, Inc., Waterloo, ON, Canada) was taped to the middle finger, 1 cm from the tip, of the active arm of each monkey; right for T and left for O. The bead was tracked optically in the infrared range (60 Hz, 0.35 mm root mean square accuracy; Polaris system, NDI). Eye position was tracked using an overhead infrared camera with an estimated accuracy of 1° (ISCAN ETL-200 Primate Eye Tracking Laboratory, ISCAN, Inc., Woburn, MA, United States). To get a stable image for the eye tracking camera, an infrared mirror (Thorlabs, Inc.) transparent to visible light was positioned at a 45° angle (facing upward) immediately in front of the nose. This reflected the image of the eye in the infrared range while allowing visible light to pass through. A visor placed around the chair prevented the monkey from touching the juice reward tube, infrared mirror, or bringing the bead to its mouth.

4.4. Task

Experiments were made up of a sequence of trials that each lasted a few seconds. Successful trials resulted in a juice reward whereas failed trials led to a time-out of 2-4 s. A trial started when a monkey held its free hand on a central circular cue (radius = 12 mm) and fixated on a small white cross (diameter = 6 mm) for ~300-485 ms. Then two isoluminant colored (red and green) targets appeared 100 mm to the left and right of the central hold cue. Targets were randomly placed such that the red target was either on the right or the left trial-to-trial, with the green target opposite the red one. In this way color was not tied to reach direction. Following an additional center hold period (400-1000 ms) a static checkerboard stimulus (15 x 15 grid of squares; 225 in total, each square: 2.5 mm x 2.5 mm) composed of isoluminant red and green squares appeared superimposed upon the fixation cross. The monkey's task was to move their hand from the center hold and touch the the target that matched the dominant color of the checkerboard stimulus for a minimum of 200 ms (full trial sequence; Fig 1B). For example, if the checkerboard stimulus was composed of more red squares than green squares the monkey had to touch the red target in order to have a successful trial. Monkeys were free to respond to the stimulus as quickly or slowly as they 'chose'. There was no delayed feedback therefore a juice reward was provided immediately following a successful trial ([Roitman and Shadlen, 2002](#)).

The checkerboard stimulus was parameterized at 14 levels of red (R) and complementing green (G) squares ranging from nearly all red (214 R , 11 G) to all green squares (11 R , 214 G) (example stimuli; Fig 1C). These 14 levels are referred to as signed coherence (SC), defined as $SC = 100 \times \frac{|R-G|}{(R+G)}$ (R : 4%:90%, G : -4%:-90%). Correspondingly there are seven levels of color coherence, agnostic to the dominant color, defined as $C = 100 \times \frac{|R-G|}{(R+G)}$ (4-90%).

The hold duration between the onset of the color targets and onset of the checkerboard stimulus was randomly chosen from a uniform distribution from 400-1000 ms for Monkey T and from an exponential distribution for Monkey O from 400-900 ms. Monkey O attempted to anticipate the checkerboard stimulus therefore an exponential distribution was chosen to minimize predictability.

4.5. Effects of coherence on accuracy and reaction time (RT)

Behavior was analyzed by fitting psychometric and RT curves on a per-session basis and averaging the results across sessions. Behavioral data was analyzed in the same sessions as the electrophysiological data. In total there were 75 sessions for monkey T (128,989 trials) and 66 sessions for monkey O (108,344 trials). On average there were \sim 1,500 trials/session. Both incorrect and correct trials for each *SC* were included for estimating RT/session.

Data were fit to a psychometric curve to characterize how discrimination accuracy changed as a function of stimulus coherence. For each session a monkey's sensitivity to the checkerboard stimulus was estimated by estimating the probability (p) of a correct choice as a function of the color coherence of the checkerboard stimulus (c). The accuracy function was fit using a Weibull cumulative distribution function.

Weibull cumulative distribution function:

$$p(c) = 1 - 0.5e^{-(\frac{c}{\alpha})^\gamma} \quad (5)$$

The discrimination threshold α is the color coherence level at which the monkey would make 81.6% correct choices. The parameter γ describes the slope of the psychometric function. Threshold and slope parameters were fit per session and averaged across sessions. We report the Mean and standard deviation of threshold and R^2 values from the fit are provided in the text.

Mean RT was calculated per *SC* on a session-by-session basis and averaged across sessions. Results are displayed in Fig 1E with error bars denoting $2 \times SEM$ and lines between the averages to guide the eyes. RT was also regressed with log coherence (c) per session. The fit coherence-RT model was used to predict RTs and calculate R^2 on a per session basis. R^2 values were averaged across sessions per monkey and are reported in Fig 1F as percentage of variance explained. The general framework and equations for linear regression and R^2 calculation are provided in section 4.9.

4.6. Electrophysiological recordings

Electrophysiological recordings were guided by stereotaxic coordinates, known response properties of PMd, and neural responses to muscle palpation. Recordings were made anterior to the central sulcus, lateral to the precentral dimple and lateral to the spur of the arcuate sulcus. Electrodes were placed in the PMd contralateral to the dominant hand of the monkey (T: right arm, O: left arm). Recording chambers were placed surface normal to the cortex to align with the skull of the monkey and recordings were performed orthogonal to the surface of the brain. Estimates of upper and lower arm representation was confirmed with repeated palpation at a large number of sites to identify muscle groups associated with the sites.

Single electrode recording techniques were used for a subset of the electrophysiological recordings. Small burr holes in the skull were made using handheld drills. A Narishige drive (Narishige International USA, Inc., Amityville, NY, United States) with a blunt guide tube was placed in contact with the dura. Sharp FHC electrodes ($> 6 M\Omega$) (FHC, Inc., Bowdoin, ME, United States) penetrated the dura and every effort was made to isolate, track, and stably record from single neurons.

180 μ m thick 16-electrode linear multi-contact electrode (U-probe (Plexon, Inc., Dallas, TX, United States); interelectrode spacing: 150 μ m, contact impedance: \sim 100 k Ω) recordings were performed similarly to single electrode recordings with some modifications. Scraping away any overlying tissue on the dura, under anesthesia, and a slightly sharpened guide tube aided in slow U-probe penetration (\sim 2-5 μ m/s). U-probe penetration was

stopped once a reasonable sample of neurons was acquired, potentially spanning multiple cortical layers. Neural responses were allowed to stabilize for 45-60 minutes before normal experimentation began. Monkey T had better recording yields on average (\sim 16 units/session) than monkey O (\sim 9 units/session). Additionally, lowering the electrode necessitated careful observation to ensure the electrode did not bend, break at the tip or excessively dimple the dura. Therefore it was not possible to precisely localize the U-probes with a grid system between sessions.

4.7. Unit selection and classification

The electrophysiological recordings consist of 996 units (546 units in T and 450 units in O, including both single neurons and multi-units) recorded from PMd of the two monkeys as they performed the task over 141 sessions. Chosen units were included as they were well isolated from other units/separated from noise and modulated activity in at least one task epoch.

U-probes were useful for recording from isolated single neurons as U-probes are low impedance (\sim 100 k Ω) with a small contact area. A conservative threshold was used to maximize the number of well defined waveforms and to minimize contamination from spurious non-neural events. Single neurons were delineated online by the 'hoops' tool of the Cerebus system software client (Blackrock Microsystems, Salt Lake City, UT, United States) after the electrodes had been in place for 30 - 45 minutes. When a spike was detected via thresholding, a 1.6 ms snippet was stored and used for subsequent evaluation of the clusters as well as modifications needed for spike sorting.

Some electrodes in U-probe recordings captured mixtures of 2 or more neurons, well separated from each other and noise. In the majority of cases the waveforms were separable and labeled as single units. These separations were verified by viewing the waveforms in principal component space using custom code in MATLAB (The MathWorks, Inc., Natick, MA, United States). MatClust the MATLAB based clustering toolbox or Plexon Offline Sorter (Plexon, Inc.) were used to adjust the clusters that were isolated online.

Recording activity labeled as 'multi-units' were mixtures of 2 or more neurons not separable using a principal components method or consisted of recordings with waveforms only weakly separable from noise.

The number of interspike interval (ISI) violations after clustering and sorting was used to mitigate subjectivity in the classification of units. A unit was labeled as a single neuron if the percentage of ISI violations (refractory period of \leq 2 ms) was \leq 1.5%, otherwise it was labeled as a multi-unit. 801/996 PMd units were labeled as single neurons (T: 417, O: 384, mean ISI violation= 0.43%, \sim 0.13 additional spikes/trial). Therefore 195/996 units were labeled as multi-unit (T: 129, O: 66, mean ISI violation= 3.36%, \sim 1.4 additional spikes/trial).

Units from both monkeys were pooled together as the electrophysiological characteristics were similar. Change-of-mind trials (\sim 2-3%) were excluded from averaging as the change in reach direction mid-movement execution made the assignment of choice ambiguous. Incorrect and correct trials arranged by choice were averaged together.

4.8. General principal component analysis (PCA) procedure of PMd firing rates

PCA was used to examine firing rate variance in the recorded PMd neural population. PCA reveals dimensions that explain a large percentage of the data while making few assumptions about the underlying structure of the data. The dimensions extracted by PCA may not always be meaningful however they often align well with behavioral variables.

The general procedure for performing a PCA involved creating a 4D matrix of all 996 units and their average firing rate activity (trial spike times censored post RT trial-by trial and convolved with 30 ms wide Gaussian kernel) windowed about checkerboard onset (\sim 600 ms: \sim 1200 ms) and organized by level of condition (e.g., coherence, RT, or past outcome) within a reach direction. Typical matrix organization was windowed firing rate \times units \times reach \times coherence/RT/past outcome (\sim 1800 \times 996 \times 2 \times 7/11/2). The raw data was centered by subtracting the mean of each column (i.e. units) and then normalized by dividing by the square root of the 99th percentile of that column (i.e. soft normalization). Soft normalization reduces the bias of units with high firing rates and ensures that each unit has roughly the same overall variability across stimulus coherences. This

data was entered into the pca function in MATLAB (The MathWorks, Inc., Natick, MA, United States). The score output from this function is used to project the dimensions that explain the most neural variance into state space.

4.9. Fits generated by linear regression and logistic regression (decoder)

Linear and logistic regressions (decoders) were respectively used to determine the variance explained by spiking activity and whether spiking activity was predictive of choice or past outcomes. Calculations were based upon U-probe sessions such that multiple neurons were recorded from at once. Therefore not all 996 units were used in these calculations. For Monkey T 24 sessions (36,690 trials) were used where there was a minimum of 9 neurons (session 61 only has 2 neurons; otherwise all other sessions ≥ 9) and a maximum of 23 neurons. For Monkey O 36 sessions (37,468 trials) were used where there was a minimum of 5 neurons in a single session and a maximum of 18 neurons. Variance explained and accuracy were averaged across both monkeys to generate the figures.

To determine whether spiking activity explains variance in RTs or predicts choice/past outcome, 1800 ms of spiking activity from each trial (600 ms prestimulus and 1200 ms post-stimulus) were divided into 20 ms bins (90 bins total) across all neurons within a session. 90 matrices composed of a single time interval of spike counts (e.g. 0-20 ms) for all trials, across all neurons were linearly/logistically regressed with trial matched RTs/choice or past outcome. Fits were used to predict RTs/choice or past outcome based on spiking activity, which were used to calculate R^2 /accuracy values per bin. The per bin R^2 /accuracy values were then averaged across sessions and compared to the 1st and 99th percentile of R^2 /accuracy values calculated from regression models of trial-shuffled (500 shuffles) spiking activity and RTs/choice or past outcome (i.e. RTs/choices or past outcomes are randomly paired with spiking activity).

Linear Regression:

$$RT(i) = b + mi \quad (6)$$

i - independent variable (i.e. coherence or binned spikes)

b - intercept

m - slope of regression

R^2 calculation:

$$R^2 = 1 - \frac{(RT_i - \widehat{RT}_i)^2}{(RT_i - \overline{RT}_i)^2} \quad (7)$$

\widehat{RT}_i - predicted RT

\overline{RT}_i - mean RT

Logistic Regression:

$$f(s_b) = \frac{1}{e^{-(as_b+b)}} \quad (8)$$

s_b - binned spiking activity

a - slope of linear equation

b - intercept of linear equation

Broyden-Fletcher-Goldfarb-Shanno quasi-Newton algorithm is used to find the optimal fit for the slope (a) and intercept (b) ([Shanno, 1970](#)). L2 regularization is used to simplify the model and decrease the collinearity of coefficients.

Cost function for logistic regression:

$$J = \frac{\lambda}{2} \sum \beta^2 \quad (9)$$

J - cost associated with coefficients

λ - penalty term

β - coefficients of the model

5 models were created via k-fold cross validation and loss was calculated for each model and accuracy is reported as $accuracy = 1 - mean(loss)$. The following equation is used to produce the outputs of the system. Either, -1 if $f(s_b) < 0.5$ or 1 if $f(s_b) > 0.5$.

4.10. Behavioral Modeling

Model equations and explanations of variables are adapted from ([Chandrasekaran and Hawkins, 2019](#)). The description of the standard drift diffusion model (DDM) (figure not shown) is presented first and presentation of the models continues in the order that they are presented in [Figure 7](#).

Standard DDM:

$$x(t + \Delta t) = x(t) + v\Delta t + s\sqrt{\Delta t} + N(0, 1) \quad (10)$$

$x(t)$ is the state of the decision-formation process at time t (i.e. decision variable), v is the drift rate (i.e. rate of sensory evidence accumulation), Δt is the time step of the process, s is the standard deviation of the moment-to-moment noise, Brownian motion, of the decision-formation process, and $N(0, 1)$ is a random sample from the standard normal distribution with a mean of 0 and standard deviation of 1. A response is made when $x(t + \Delta t) \geq a_{upper}$ or $x(t + \Delta t) \leq a_{lower}$. Whether a response is correct or not is determined from the boundary that was crossed and the sign of the drift rate. $v > 0$ implies the upper boundary corresponds to the correct response and $v < 0$ implies that the lower boundary corresponds to the incorrect response. For simplicity $a_{lower} = 0$ & $a_{upper} = A$.

DDM with variable drift rate (v_{ij}), starting point (s_z), and non-decision time ($T_{er,j}$):

$$x_j(t + \Delta t) = x_j(t) + v_{ij}\Delta t + s\sqrt{\Delta t} + N(0, 1) \quad (11)$$

$$x_j(0) \sim U(z - \frac{s_z}{2}, z + \frac{s_z}{2}) \quad (12)$$

$$v_{ij} \sim N(v_i, s_v) \quad (13)$$

$$T_{er,j} \sim U(T_{er} - \frac{s_t}{2}, T_{er} + \frac{s_t}{2}) \quad (14)$$

The decision variable ($x_j(t + \Delta t)$) has a variable drift rate (v_{ij}) which varies as a function of condition (i) and particular trial (j). The initial value of the decision variable ($x_j(0)$) has a variable starting point (z - midpoint between bounds, s_z - variable start point constant) determined from a uniform distribution (U). The variable condition and trial variable drift rate is pulled from a normal distribution (N) with a mean of the condition average drift rate (v_i) and standard deviation is the variable drift rate constant (s_v). The trial variable non-decision time ($T_{er,j}$) is pulled from a uniform distribution with a range determined by the constant non-decision time (T_{er}) and variable non-decision time constant (s_t).

DDM with collapsing bounds:

$$a_{lower}(t) = a(1 - e^{(\frac{t}{\lambda})^k})(0.5 - a') \quad (15)$$

$$a_{upper}(t) = a - a_{lower}(t) \quad (16)$$

$a_{lower/upper}(t)$ - position of the lower/upper boundary at time t

a - initial position of upper boundary at $t=0$

a' - asymptotic boundary setting (where lower and upper boundary meet; $a' = 0.5$)

λ - scale parameter of Weibull distribution

k - shape parameter of Weibull distribution; the Weibull function is used here to determine the shape of the collapsing bounds as the function can approximate different distributions (e.g. exponential) ([Chandrasekaran and Hawkins, 2019](#)).

DDM with variable urgency signal:

$$E(t) = v\Delta t + s\sqrt{\Delta t}N(0, 1) \quad (17)$$

$$x(t + \Delta t) = x(t) + E(t)\gamma(t) \quad (18)$$

$$\gamma_j(t) = b_j + m_j t \quad (19)$$

$$\gamma_j(t) = b_j + m_j(1 - e^{(\frac{-t}{\lambda})^k}) \quad (20)$$

$$b_j \sim U(b - \frac{s_b}{2}, b + \frac{s_b}{2}) \quad (21)$$

$$m_j \sim U(m - \frac{s_m}{2}, m + \frac{s_m}{2}) \quad (22)$$

$E(t)$ - momentary sensory evidence at time t

$\gamma(t)$ - magnitude of urgency signal at time t

b_j - trial variable urgency intercept (chosen from a uniform distribution)

s_b - variable intercept constant

m_j - trial variable urgency slope (chosen from a uniform distribution)

s_m - variable slope constant

λ - scale parameter of sigmoid

k - shape parameter of sigmoid

4.11. Calculation of AIC and BIC

Three different measures for model selection were calculated to test the goodness of fit of behavioral models for RT and accuracy data. First an approximation to the maximum likelihood estimation, Quantile Maximum Products statistic (Heathcote et al., 2002), is calculated and used to calculate Akaike Information Criterion (AIC) and Bayesian Information Criterion (BIC). AIC and BIC are similar in calculation, differing in the size of the penalty term for model complexity, and are therefore used to distinct ends (Chandrasekaran and Hawkins, 2019; Aho et al., 2014). AIC (Akaike, 1974) is useful for model exploration when the expectation is that models will grow in complexity with increased sample size. AIC treats false negatives as worse than false positives with a lesser penalty for model complexity than BIC and is used to judge between models that are assumed to be incorrect (Chandrasekaran and Hawkins, 2019; Aho et al., 2014). BIC (Schwarz, 1978) on the other hand treats false positives more harshly with a larger penalty term for extra parameters. The expectation here is that the correct model has been chosen and that the model will stabilize with increased sample size (Chandrasekaran and Hawkins, 2019; Aho et al., 2014). Lower AIC & BIC and higher log-likelihood, respectively, indicate better model approximation of the actual data. These scores are not objective measures of a model's goodness of fit but rather are meant to be used as a comparison between different models.

Akaike Information Criterion (AIC):

$$AIC = 2k - 2\ln(\hat{L}) \quad (23)$$

k - number of model parameters

\hat{L} - maximized value of the likelihood function

Bayesian Information Criterion (BIC):

$$BIC = k\ln(n) - 2\ln(\hat{L}) \quad (24)$$

k - number of model parameters

n - sample size

\hat{L} - maximized value of the likelihood function

4.12. Kinematic analysis of neural trajectories (KiNeT)

KiNeT (Remington et al., 2018) was used in order to characterize how state space trajectories evolve over time in terms of relative speed and position as compared to a reference trajectory. The analysis was performed on the dynamics from the PCA on unit averaged firing rates conditioned on choice and RT/past outcome. This allowed the determination of whether certain RT/past outcome states were associated with faster or slower dynamics.

The first 6 PCs (~90% of variance) were chosen as the Euclidean coordinate system, as these PCs were significantly different from noise (Machens et al., 2010). Next we chose the trajectory associated with the middle RT bin (cyan, Fig 4C) as the 'reference' trajectory (Ω_{ref}). To find speed (t_i - time in relation to a reference, $t_i < 0$ faster, $t_i > 0$ slower) of trajectories we found the minimum Euclidean distance (e.g. $\text{argmin}||\cdot||$) for all points on all non-reference trajectories from the corresponding points on the reference trajectory. Time (t_i) was used to find the corresponding positions (s_i) on the non-reference trajectories and the normalized difference between the reference trajectory position and non-reference trajectory was used to find the distance (D_i).

Non-reference time in relation to reference time (i.e. speed) (t_i):

$$t_i[j] = \text{argmin}_\tau ||\Omega_i(\tau) - s_{ref}[j]|| \quad (25)$$

Position of non-reference trajectory in relation to reference trajectory (s_i):

$$s_i[j] = \Omega_i(t_i[j]) \quad (26)$$

Distance of non-reference trajectory from reference trajectory (D_i):

$$D_i[j] = \|s_{ref}[j] - s_i[j]\| \quad (27)$$

i - non-reference trajectories

j - location on trajectory

Ω_i - non-reference trajectory

τ - time associated with position j on reference trajectory

$\Omega_i(\tau)$ - position of non-reference trajectory at corresponding time on reference trajectory

s_{ref} - position of reference trajectory at point j

$argmin$ - where function achieves its minimum at point j

4.13. Latent Factors Analysis of Dynamical Systems (LFADS)

Briefly, LFADS is a generative model which assumes that neuronal spiking activity is generated from an underlying dynamical system ([Pandarinath et al., 2018](#)). This dynamical system is assumed to be relatively low-dimensional (i.e. considerably smaller than the number of neurons involved) and latent factors can be extracted and exploited to recreate spiking activity on single trials. This method uses a trained autoencoder to generate ‘initial conditions’ based on a trial’s neurons’ spike counts. This ‘latent code’ serves as the initial condition to the generator RNN. From the latent code the generator infers the latent factors of all the neurons in that trial. Here LFADS was used for a single session which recorded from 23 neurons. Our model consisted of 8 latent factors to recreate spiking activity of single trials with the first 3 factors were visualized in [Fig 5 A, E](#). Please refer to Pandarinath and colleagues, 2018 for a full description of the LFADS method.

References

- Afshar, A., Santhanam, G., Yu, B. M., Ryu, S. I., Sahani, M., and Shenoy, K. V. (2011). Single-trial neural correlates of arm movement preparation. *Neuron*, 71:555–564.
- Aho, K., Derryberry, D., and Peterson, T. (2014). Model selection for ecologists: the worldviews of aic and bic. *Ecology*, 95:631–636.
- Akaike, H. (1974). A new look at the statistical model identification. *IEEE Transactions on Automatic Control*, 19:716–723.
- Bahl, A. and Engert, F. (2020). Neural circuits for evidence accumulation and decision making in larval zebrafish. *Nature Neuroscience*, 23:94–102.
- Bogacz, R., Wagenmakers, E.-J., Forstmann, B. U., and Nieuwenhuis, S. (2010). The neural basis of the speed-accuracy tradeoff. *Trends in Neurosciences*, 33:10–16.
- Briggman, K. L., Abarbanel, H. D. I., and Kristan, W. B. (2005). Optical imaging of neuronal populations during decision-making. *Science*, 307:896–901.
- Brody, C. D. and Hanks, T. D. (2016). Neural underpinnings of the evidence accumulator. *Current Opinion in Neurobiology*, 37:149–157.
- Brunton, B. W., Botvinick, M. M., and Brody, C. D. (2013). Rats and humans can optimally accumulate evidence for decision-making. *Science*, 340:95–98.
- Chandrasekaran, C. and Hawkins, G. E. (2019). Chartr: An r toolbox for modeling choices and response times in decision-making tasks. *Journal of Neuroscience Methods*, 328:108432.
- Chandrasekaran, C., Peixoto, D., Newsome, W. T., and Shenoy, K. V. (2017). Laminar differences in decision-related neural activity in dorsal premotor cortex. *Nature Communications*, 8:614.
- Churchland, A. K., Kiani, R., and Shadlen, M. N. (2008). Decision-making with multiple alternatives. *Nature Neuroscience*, 11:693–702.
- Churchland, M. M., Afshar, A., and Shenoy, K. V. (2006a). A central source of movement variability. *Neuron*, 52:1085–1096.
- Churchland, M. M., Cunningham, J. P., Kaufman, M. T., Ryu, S. I., and Shenoy, K. V. (2010). Cortical preparatory activity: Representation of movement or first cog in a dynamical machine? *Neuron*, 68:387–400.
- Churchland, M. M., Yu, B. M., Ryu, S. I., Santhanam, G., and Shenoy, K. V. (2006b). Neural variability in premotor cortex provides a signature of motor preparation. *Journal of Neuroscience*, 26:3697–3712.
- Cisek, P. (2012). Making decisions through a distributed consensus. *Current Opinion in Neurobiology*, 22:927–936.
- Cisek, P., Puskas, G. A., and El-Murr, S. (2009). Decisions in changing conditions: The urgency-gating model. *Journal of Neuroscience*, 29:11560–11571.
- Danielmeier, C. and Ullsperger, M. (2011). Post-error adjustments. *Frontiers in Psychology*, 2.
- Ding, L. and Gold, J. I. (2010). Caudate encodes multiple computations for perceptual decisions. *Journal of Neuroscience*, 30:15747–15759.

- Ferguson, K. A. and Cardin, J. A. (2020). Mechanisms underlying gain modulation in the cortex. *Nature Reviews Neuroscience*, 21:80–92.
- Ghazanfar, A. A. and Santos, L. R. (2004). Primate brains in the wild: the sensory bases for social interactions. *Nature Reviews Neuroscience*, 5:603–616.
- Gold, J. I. and Shadlen, M. N. (2007). The neural basis of decision making. *Annual Review of Neuroscience*, 30:535–574.
- Goris, R. L., Movshon, J. A., and Simoncelli, E. P. (2014). Partitioning neuronal variability. *Nature Neuroscience*, 17:858–865.
- Groschner, L. N., Hak, L. C. W., Bogacz, R., DasGupta, S., and Miesenböck, G. (2018). Dendritic integration of sensory evidence in perceptual decision-making. *Cell*, 173:894–905.e13.
- Guo, Z. V., Li, N., Huber, D., Ophir, E., Gutnisky, D., Ting, J. T., Feng, G., and Svoboda, K. (2014). Flow of cortical activity underlying a tactile decision in mice. *Neuron*, 81:179–194.
- Hanks, T., Kiani, R., and Shadlen, M. N. (2014). A neural mechanism of speed-accuracy tradeoff in macaque area lip. *eLife*, 3.
- Hanks, T. D., Kopec, C. D., Brunton, B. W., Duan, C. A., Erlich, J. C., and Brody, C. D. (2015). Distinct relationships of parietal and prefrontal cortices to evidence accumulation. *Nature*, 520:220–223.
- Hanks, T. D. and Summerfield, C. (2017). Perceptual decision making in rodents, monkeys, and humans. *Neuron*, 93:15–31.
- Heathcote, A., Brown, S., and Mewhort, D. J. K. (2002). Quantile maximum likelihood estimation of response time distributions. *Psychonomic Bulletin & Review*, 9:394–401.
- Heitz, R. P. and Schall, J. D. (2012). Neural mechanisms of speed-accuracy tradeoff. *Neuron*, 76:616–628.
- Jacobs, E. A., Steinmetz, N. A., Peters, A. J., Carandini, M., and Harris, K. D. (2020). Cortical state fluctuations during sensory decision making. *Current Biology*, 30:4944–4955.e7.
- Kato, S., Kaplan, H. S., Schrödel, T., Skora, S., Lindsay, T. H., Yemini, E., Lockery, S., and Zimmer, M. (2015). Global brain dynamics embed the motor command sequence of *caenorhabditis elegans*. *Cell*, 163:656–669.
- Kelly, S. P. and O'Connell, R. G. (2013). Internal and external influences on the rate of sensory evidence accumulation in the human brain. *Journal of Neuroscience*, 33:19434–19441.
- Kiani, R., Churchland, A. K., and Shadlen, M. N. (2013). Integration of direction cues is invariant to the temporal gap between them. *Journal of Neuroscience*, 33:16483–16489.
- Kriegeskorte, N. and Kievit, R. A. (2013). Representational geometry: integrating cognition, computation, and the brain. *Trends in Cognitive Sciences*, 17:401–412.
- Lakatos, P., Karmos, G., Mehta, A. D., Ulbert, I., and Schroeder, C. E. (2008). Entrainment of neuronal oscillations as a mechanism of attentional selection. *Science*, 320:110–113.
- Lara, A. H., Elsayed, G. F., Zimnik, A. J., Cunningham, J. P., and Churchland, M. M. (2018). Conservation of preparatory neural events in monkey motor cortex regardless of how movement is initiated. *eLife*, 7.
- Latimer, K. W., Yates, J. L., Meister, M. L. R., Huk, A. C., and Pillow, J. W. (2015). Single-trial spike trains in parietal cortex reveal discrete steps during decision-making. *Science*, 349:184–187.

- Machens, C. K., Romo, R., and Brody, C. D. (2010). Functional, but not anatomical, separation of "what" and "when" in prefrontal cortex. *Journal of Neuroscience*, 30:350–360.
- Mante, V., Sussillo, D., Shenoy, K. V., and Newsome, W. T. (2013). Context-dependent computation by recurrent dynamics in prefrontal cortex. *Nature*, 503:78–84.
- Murphy, P. R., Boonstra, E., and Nieuwenhuis, S. (2016). Global gain modulation generates time-dependent urgency during perceptual choice in humans. *Nature Communications*, 7:13526.
- Murty, N. A. R. and Arun, S. P. (2018). Multiplicative mixing of object identity and image attributes in single inferior temporal neurons. *Proceedings of the National Academy of Sciences of the United States of America*, 115:E3276–E3285.
- Okazawa, G., Hatch, C. E., Mancoo, A., Machens, C. K., and Kiani, R. (2021). Representational geometry of perceptual decisions in the monkey parietal cortex. *Cell*, 184:3748–3761.e18.
- Pandarinath, C., O'Shea, D. J., Collins, J., Jozefowicz, R., Stavisky, S. D., Kao, J. C., Trautmann, E. M., Kaufman, M. T., Ryu, S. I., Hochberg, L. R., Henderson, J. M., Shenoy, K. V., Abbott, L. F., and Sussillo, D. (2018). Inferring single-trial neural population dynamics using sequential auto-encoders. *Nature Methods*, 15:805–815.
- Pastalkova, E., Itskov, V., Amarasingham, A., and Buzsáki, G. (2008). Internally generated cell assembly sequences in the rat hippocampus. *Science*, 321:1322–1327.
- Pereira, M., Megevand, P., Tan, M. X., Chang, W., Wang, S., Rezai, A., Seeck, M., Corniola, M., Momjian, S., Bernasconi, F., Blanke, O., and Faivre, N. (2021). Evidence accumulation relates to perceptual consciousness and monitoring. *Nature Communications*, 12:3261.
- Purcell, B. A. and Kiani, R. (2016). Neural mechanisms of post-error adjustments of decision policy in parietal cortex. *Neuron*, 89:658–671.
- Rabinowitz, N. C., Goris, R. L., Cohen, M., and Simoncelli, E. P. (2015). Attention stabilizes the shared gain of v4 populations. *eLife*, 4.
- Ratcliff, R. (1978). A theory of memory retrieval. *Psychological Review*, 85:59–108.
- Remington, E. D., Narain, D., Hosseini, E. A., and Jazayeri, M. (2018). Flexible sensorimotor computations through rapid reconfiguration of cortical dynamics. *Neuron*, 98:1005–1019.e5.
- Roitman, J. D. and Shadlen, M. N. (2002). Response of neurons in the lateral intraparietal area during a combined visual discrimination reaction time task. *The Journal of Neuroscience*, 22:9475–9489.
- Schwarz, G. (1978). Estimating the dimension of a model. *The Annals of Statistics*, 6:461–464.
- Shadlen, M. N. and Newsome, W. T. (1996). Motion perception: seeing and deciding. *Proceedings of the National Academy of Sciences*, 93:628–633.
- Shadlen, M. N. and Newsome, W. T. (2001). Neural basis of a perceptual decision in the parietal cortex (area lip) of the rhesus monkey. *Journal of Neurophysiology*, 86:1916–1936.
- Shanno, D. F. (1970). Conditioning of quasi-newton methods for function minimization. *Mathematics of Computation*, 24:647.
- Shenoy, K. V., Sahani, M., and Churchland, M. M. (2013). Cortical control of arm movements: A dynamical systems perspective. *Annual Review of Neuroscience*, 36:337–359.

- Stroud, J. P., Porter, M. A., Hennequin, G., and Vogels, T. P. (2018). Motor primitives in space and time via targeted gain modulation in cortical networks. *Nature Neuroscience*, 21:1774–1783.
- Thura, D., Cabana, J.-F., Feghaly, A., and Cisek, P. (2020). Unified neural dynamics of decisions and actions in the cerebral cortex and basal ganglia. *bioRxiv*, page 2020.10.22.350280.
- Thura, D. and Cisek, P. (2014). Deliberation and commitment in the premotor and primary motor cortex during dynamic decision making. *Neuron*, 81:1401–1416.
- Thura, D., Guberman, G., and Cisek, P. (2017). Trial-to-trial adjustments of speed-accuracy trade-offs in premotor and primary motor cortex. *Journal of Neurophysiology*, 117:665–683.
- van den Brink, R. L., Wynn, S. C., and Nieuwenhuis, S. (2014). Post-error slowing as a consequence of disturbed low-frequency oscillatory phase entrainment. *Journal of Neuroscience*, 34:11096–11105.
- Williams, A. H. and Linderman, S. W. (2021). Statistical neuroscience in the single trial limit. *Current Opinion in Neurobiology*, 70:193–205.
- Zagha, E., Erlich, J. C., Lee, S., Lur, G., O'Connor, D. H., Steinmetz, N. A., Stringer, C., and Yang, H. (2022). The importance of accounting for movement when relating neuronal activity to sensory and cognitive processes. *The Journal of Neuroscience*, pages JN-TS-1919–21.

5. Supplemental materials

5.1. PCA analyses of firing rates suggest an organized covariation with coherence and choice

PCAs on trial-averaged firing rates conditioned on coherence and choice, and another conditioned on RT and choice were performed to make sense of this heterogeneous population of neurons with time-varying firing rates and to extract signals associated with decision-making.

First, to understand how neural activity was organized by coherence and choice, a PCA of firing rate activity from all 996 neurons conditioned by the two reach directions and the 7 levels of coherence was conducted ($1800 \times 996 \times 2 \times 7$) (SFig 1). The first principal component (PC) explains $\sim 50\%$ of the variance and appears to represent the change in firing rates after stimulus onset (SFig 1A), panel 1). The second PC explains $\sim 15\%$ of the variance and separates convincingly on choice and then on stimulus difficulty within a choice at ~ 200 ms post-stimulus onset (SFig 1A), panel 2). The first 4 PCs explain $> 80\%$ of the variance (SFig 1C). Observe how activity separates as a function of choice as well as coherence when the first three PCs are plotted in state space (SFig 1B). In this 3D space, activity separates faster for easier compared to harder choices. This result is reassuring as it recapitulates findings from classical studies done in single neurons, at the population level (Shadlen and Newsome, 2001; Roitman and Shadlen, 2002; Ding and Gold, 2010).

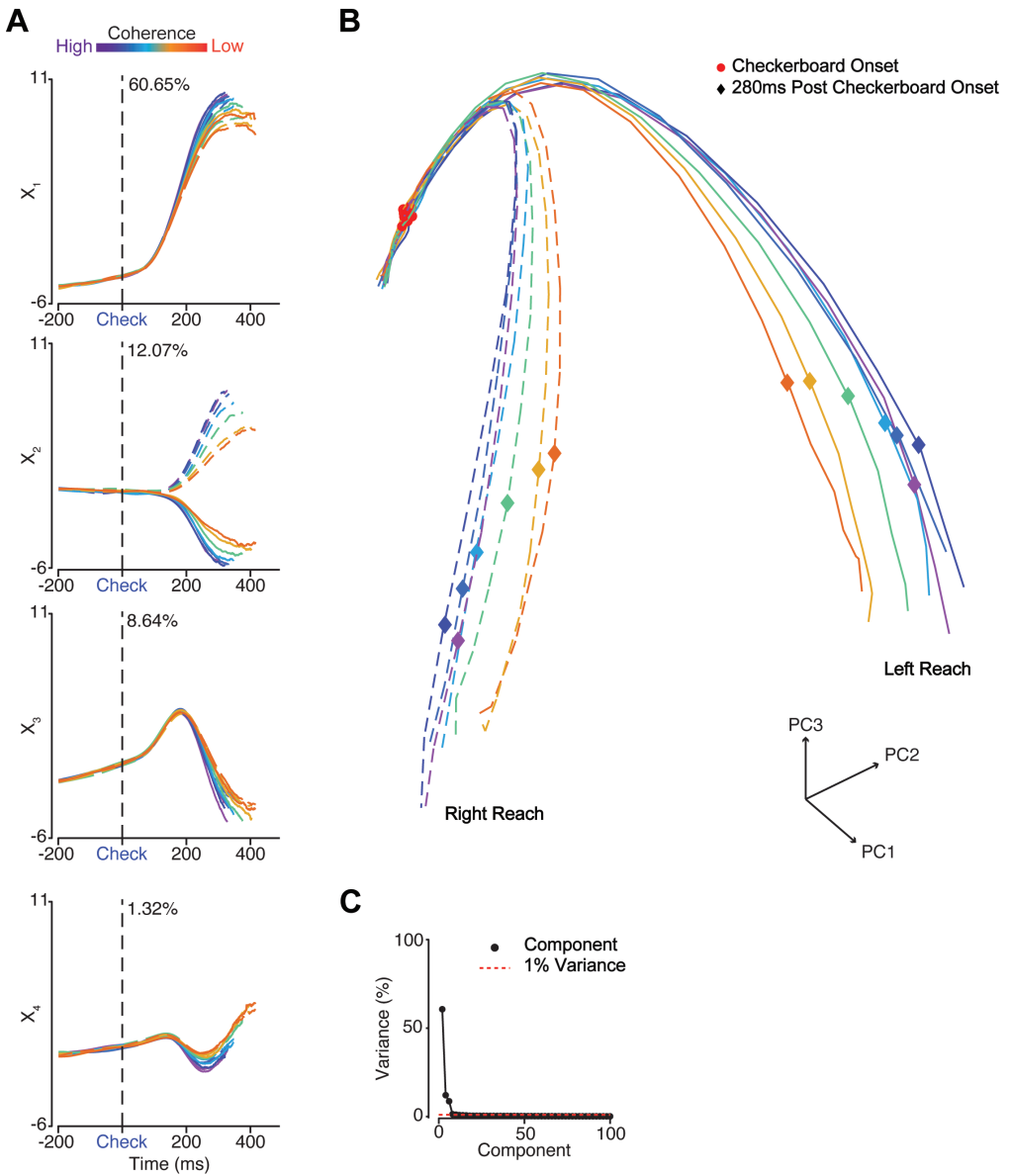


Figure 8: Principal components of neural firing rates separate lawfully by choice and coherence (A) The first 4 PCs ($X_{1,2,3,4}$) of trial averaged firing rates of all 996 neurons from monkeys T & O and all sessions organized across 7 levels of color coherence (purple - easiest coherence to red - hardest coherence), both reach directions (right - dashed, left - solid), and aligned to checkerboard onset ('Check' & black dashed line). Percentage variance explained by each PC presented at the top of each plot. (B) 3D structure (i.e. state space) of the first 3 PCs ($X_{1,2,3}$) aligned to checkerboard onset (red dots). PC 1/2/3 - principal component 1/2/3. Different colored diamonds indicate 280 ms post-checkerboard onset. Observe how neural activity separates as a function of choice and coherence < 200 ms post stimulus onset. Notice that the plotting of PCs extends 200 ms before checkerboard onset. (C) Scree plot of the percentage of variance explained by the first 50 components. Black dots represent each component plotted in order of the amount of variance explained. The red dotted line denotes 1% of variance and black dots that fall below this explain less than 1% of variance. The first 3 PCs already capture $> 80\%$ of the variance in the firing rate activity, with the 4th component only explaining just over 1% of the variance.